공학박사 학위논문

Dynamics of Magnetic Vortices Coupled in Magnetic Disk Array

자성 디스크 배열 내 결합된 자기 소용돌이의 동적 거동 연구

2020 년 2 월

서울대학교 대학원

공과대학 재료공학부

조 영 준

자성 디스크 배열 내 결합된 자기 소용돌이의 동적 거동 연구

Dynamics of Magnetic Vortices Coupled in Magnetic Disk Array

지도 교수: 김상국

이 논문을 공학박사 학위논문으로 제출함

2020 년 2 월

서울대학교 대학원

공과대학 재료공학부

조 영 준

조영준의 공학박사 학위논문을 인준함

2020 년 1 월

위 원 장	홍 성 현	(인)
부 위 원 장	김 상 국	(인)
위 원	김 미 영	(인)
위 원	김 상 범	(인)
위 원	한 동 수	(인)

Dynamics of Magnetic Vortices Coupled in Magnetic Disk Array

A THESIS
SUBMITTED TO THE FACULTY OF SEOUL NATIONAL UNIVERSTY
BY

Young-Jun Cho

Supervised by

Prof. Sang-Koog Kim

IN PARTIAL FULFILLMENT OF THE REQUIREMENTS FOR THE DEGREE OF DOCTOR OF PHILOSOPHY

February 2020

Department of Materials Science and Engineering Graduate School Seoul National University

Abstract

Dynamics of Magnetic Vortices Coupled in Magnetic Disk Array

Young-Jun Cho

Department of Materials Science and Engineering

Seoul National University

In the sub-micrometer-size ferromagnetic structure, the magnetic vortex is in a strongly stable ground state characterized by an in-plane curling magnetization around and an out-of-plane magnetization in the central region. The magnetic vortex is characterized by clockwise (CW) or counter-clockwise (CCW) curling in-plane magnetizations around a single vortex core in which region magnetizations are perpendicularly oriented either upward or downward. In isolated disks, applied external forces induce vortex excitations, among which a translational mode exists in which the vortex core gyrates around its equilibrium position at a characteristic eigenfrequency. Vortex-core switching can be accomplished with low power consumption when vortex gyrations are resonantly excited. Moreover, the gyration modes of individual vortex cores in a periodic array of patterned vortex-state disks are coupled with each other, thus yielding collectively coupled motions of the individual cores. On the basis of such novel dynamic characteristics, non-volatile memory and information processing devices using magnetic vortex have been proposed.

This work focused on dynamic interaction between vortex-state ferromagnetic structures and its applications, utilizing micromagnetic simulations, analytical calculations, and experiments. The dynamic behaviors of vortex-gyration-coupled modes, vortex-core switching, and propagation of vortex-core gyration signal in magnetic-disk-network devices are investigated. Based on the combinations of the novel dynamic characteristics of vortices in dipolar-coupled disks, a new concept RS latch logic, time- and frequency-division demultiplexer device operations are explored. Magnetic vortex has many advantages such as non-volatility, almost unlimited endurance, and low power operation. Furthermore, a rich tunability of magnetic vortices makes them adoptable as future spintronics devices. This work can pave the way for possible implementation of logic gates and information processing devices based on coupled magnetic vortices.

Keywords: magnetic vortex, vortex dynamics, coupled dynamics, vortex switching, spin dynamics, magnonic crystal, spin wave, spintronics

Student Number: 2012-30920

Contents

List of Tables

List of Figures

1. Introduction

The electron charge and its flow in nanoscale channels are the key functionalities in current information-storage and -processing technologies. The inevitable disadvantages are the leakage and energy loss of electrons flowing in complex nano-scale channels and circuits. These problems have stimulated a great number of studies on the search for novel alternative materials, new device concepts, and computational paradigm shifts along with more functional and less power-consuming devices in order to overcome the constraints inherent to the complementary metal-oxide-semiconductor (CMOS)-based circuitry.

The ability to study and manipulate the magnetic properties of matter on an increasingly smaller scale is an important feature of modern magnetism. Since IBM introduced the first hard disk drive with the RAMAC project in the 1950s, the research leading to such advances has largely been stimulated by the rapid progress accomplished in information technology and the need for high-density non-volatile storage media ever. Scientific curiosity is the origin of most advances in understanding magnetism. In this context, the discovery of giant magnetoresistance (GMR) [1, 2], for which the 2007 Nobel Prize was awarded to Grünberg and Fert, was one of the notable examples of the impact of basic science research. The discovery that the resistance of a layered magnetic thin film separated by a nonmagnetic layer has high dependency on the relative direction of magnetization of each layer rapidly evolved from an interesting physical phenomena to changed applications [3, 4] in information technology.

In the meantime, in the growth of high quality thin films of ferromagnetic materials

combined with advances in modern nano-lithography technology has recently progressed, making it a subject of renewed interest. From the basic perspective of research in magnetization dynamics, spin-wave can now be studied in individual nanostructures with complex spatial non-uniform ground state. This progress also opens up the possibility of controlling and manipulating the magnetization of small objects.

The dynamic properties of these ferromagnetic micro- and nano-objects have gained a broad scientific interest: concepts of high-density and ultrafast nonvolatile data storage devices [5,6], information-signal processing devices [7,8], logical devices [9,10], and microwave emission sources [11,12]. The properties of these ferromagnetic micro- and nano-objects are largely different from those of bulk magnets. A remarkable structure arising from magnetic confinement is the vortex. In ferromagnetic materials with finite geometries, magnetization tends to form domains that close the magnetic flux [13]. In the center of such flux structures, there is often an area of just a few nanometers in size forming a magnetic vortex, where the magnetization circulates around a core. At the core, in order to avoid a singularity of the exchange energy density, the magnetization lifts out of the plane. While this structure was predicted over fifty years ago, it has been confirmed experimentally using MFM twenty years ago [14, 15].

Magnetic vortex configuration [14,15] is known to show unique properties in its collective dynamics among various types of magnetic domains. Magnetic vortex possesses a low frequency mode approximated as dynamics of a rigid quasiparticle in a parabolic potential [16,17] and its spatial symmetry is reversed by changing a part of magnetization structure core polarization. These features are unique for a model system,

and various proposals of vortex used novel type of spintronics devices have been proposed [11, 18-21]. Among them, stray field mediated interaction between neighboring vortices directly reflect on this switchable spatial symmetry [22-24], and can be used for artificial molecules exploiting spin wave propagation, so called magnonic crystal [25-28].

The aim of this thesis is to explore fundamental aspects of the magnetization dynamics of magnetic vortex in coupled ferromagnetic disks, in particular the method to control the collective magnetization dynamics. The presented results are based on numerical simulations performed within the framework of micromagnetic theory. The theory describes the static and dynamic properties of the magnetization in mesoscopic and nanoscale ferromagnetic materials.

This thesis is organized as follows. Chapter 2 describes theoretical and experimental background of this research. Theory will be extended to describe the dynamics in confined magnetic structures in the vortex state. Controlling the vortex states and effective switching of the vortex core polarity will be explained. The interaction between dipolar-coupled vortex and its dynamics will also be introduced. After that, the background for sample preparation and electrical measurement experiment will be introduced. Chapter 3 reports an alternative way of vortex-core switching by propagation of a specific gyration-coupled mode transferred from the neighboring disks by micromagnetic simulations. Based on the results, a new concept of RS(reset-set) latch logic device was proposed and its operational characteristics are explored. Chapter 4 reports a control method of gyration signal propagation by in-plane field and switching core polarity in the magnetic disk arrays by micromagnetic simulations. The results are

used to propose a new concept of demultiplexer device based on magnetic vortex. Chapter 5 reports experimental results of electrically measured gyrotropic motion of magnetic vortex core. The detailed descriptions of techniques and processes used for sample fabrication and the electrical measurement setups are given. Photo- and electron-beam-lithography techniques used to pattern structures on the nano-scale will be described. The measurement setups used to investigate magnetic vortices electrically utilizing AMR (Anisotropic Magnetoresistance) phenomenon will be described in detail. The thesis closes with a conclusion in chapter 6.

2. Research Background

2.1. Magnetization dynamics and micromagnetics

The history of micromagnetics starts from Landau and Lifshitz [29], and developed mainly by Brown [30]. Micromagnetics cover the relevant physics describing the behavior of the magnetization in ferromagnets on length scales large enough to approximate the underlying atomic structure with a continuum model. Micromagnetics is able to describe structures like domain walls and magnetic vortices that are too large to be described in a quantum mechanical model, since the exchange interaction can also be implemented on a classical dynamics length scale. Nowadays, the micromagnetics are one of the most powerful tools for understanding of static and dynamic behavior of spins in confined magnetic media.

2.1.1. Landau-Lifshitz-Gilbert equation

After Landau and Lifshitz derived a differential equation for the dynamics of the magnetization process, later it was extended by Gilbert and the corresponding equation of motion for the magnetization dynamics is nowadays known as the Landau-Lifshitz-Gilbert (LLG) equation [31]:

$$\frac{d\mathbf{M}}{dt} = -\gamma \mathbf{M} \times \mathbf{H}_{eff} + \frac{\alpha}{M_s} \mathbf{M} \times \frac{d\mathbf{M}}{dt} \qquad (2.1.1)$$

The LLG equation describes the dynamics of individual magnetic moments interacting with each other through dipolar coupling, exchange interaction, magnetocrystalline anisotropy, and Zeeman field. The first term on the right hand side presents the

precession of the magnetization around the effective magnetic field. This term conserves the energy of the system. The precession rate is propotional to the field **H**, with the gyromagnetic ration which is given by $\gamma = \frac{\mu_0 g e}{2m_e}$: g is the Lande g-factor, μ_0 is the permeability of free space, e and m_e are the charge and mass of the electron, respectively. The second term is the damping term which describes the energy loss during magnetization precession.

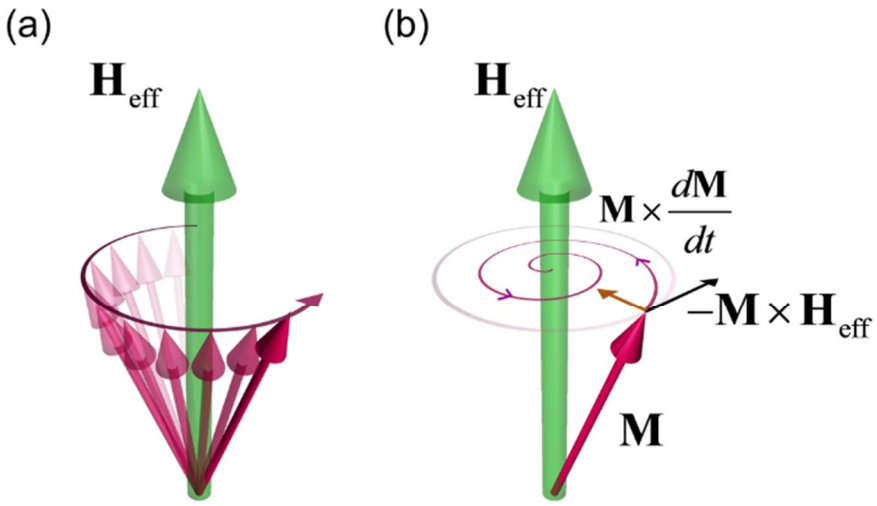

Fig 2.1 Schematic illustration of magnetization precession motion around the effective field (a) without damping and (b) with damping, adopted from [32].

2.1.2. Effective fields in the LLG equation

In the Landau-Lifshitz-Gilbert equation, the effective field is a sum of exchange field, anisotropy field, demagnetization field, and Zeeman field. The exchange energy is caused from the interaction among electron spins. Heisenberg generalized the exchange Hamiltonian [33]:

$$H = -J\mathbf{S}_i \cdot \mathbf{S}_j = -J\left|\mathbf{S}_i\right|\left|\mathbf{S}_j\right|\cos\phi \quad (2.1.2)$$

where J is the exchange constant. When the cosine is expanded into a Taylor series assuming only small angles between the spins and the zero of the total energy is shifted by the constant term $-J\left|\mathbf{S}_i\right|\left|\mathbf{S}_j\right|$, the exchange energy density reads

$$\hat{H} = \frac{J}{a^3}\mathbf{S}_i \cdot \mathbf{S}_j\left(\frac{\phi^2}{2}\right) \approx \frac{J}{2M_s^2 \cdot a}\left(\nabla\mathbf{M}\right)^2 = \frac{A}{M_s^2}\left(\nabla\mathbf{M}\right)^2 \quad (2.1.3)$$

where a is the lattice constant, ϕ is the angle between the spins, M_s is the saturation magnetization, and $A = J/2a$ is the exchange constant. The exchange energy of a ferromagnetic system can be obtained from a volume integration of equation (2.1.3) as follows.

$$E_{ex} = \frac{A}{M_s^2}\int\left(\nabla\mathbf{M}\right)^2 dV \quad (2.1.4)$$

And the exchange field can be calculated from the functional derivative of the exchange energy.

$$H_{ex} = \frac{2A}{\mu_0 M_s^2}\nabla^2\mathbf{M} \quad (2.1.5)$$

The demagnetization field in a ferromagnetic body is derived by the Maxwell equations $\nabla \times \mathbf{H}_d = 0$ and $\nabla \cdot \mathbf{B}_d = 0$ [34]. The change of magnetic scalar potential at inside and outside magnetic bodies are $\Delta U_{\text{in}} = \nabla \cdot \mathbf{M}$ and $\Delta U_{\text{out}} = 0$, respectively. Boundary conditions on the surface to obtain U, H are $U_{\text{in}} = U_{\text{out}}$ and $\partial U_{\text{in}} / \partial n - \partial U_{\text{out}} / \partial n = \mathbf{M} \cdot \mathrm{n}$ [31]. As the results, the demagnetization field and energy can be derived as follows:

$$\mathbf{H}_d = -\int \mathbf{N}(\mathbf{r} - \mathbf{r}')\mathbf{M}(\mathbf{r}')dV' \quad (2.1.6)$$

$$\mathbf{E}_d = -\frac{\mu_0}{2}\int \mathbf{H}_d \cdot \mathbf{M}(\mathbf{r})dV \quad (2.1.7)$$

with a demagnetization tensor **N**. Zeeman energy with the Zeeman field $\mathrm{H}_{\mathrm{Zeeman}}$ reads

$$\mathbf{E}_{Zeeman} = -\mu_0 \int \mathbf{H}_{Zeeman} \cdot \mathbf{M}dV \quad (2.1.8)$$

2.2. Vortices in magnetic microstructures and their dynamics

The magnetic vortex [35-38] is a stable ground state configuration in micron and sub-micron sized soft ferromagnetic thin film structures. Such elements are magnetized in-plane because of the predominant influence of the dipolar energy (and the shape anisotropy). By aligning the magnetic moments parallel to the edges, surface charges at the boundary of the structure are avoided, and exchange interactions cause neighboring spins in the inner region to align in parallel with the spins the outer region, which results to form a flux-closure pattern. The sense of the in-plane flux closure is called the chirality c and could take two possible values: c = +1 (counter-clock-wise orientation) and c = −1 (clock-wise orientation). As one approaches the center of the magnetic element, adjacent spins inevitably align in antiparallel. In order to avoid a singularity in the center of the structure and to minimize the exchange energy, the spins tilt out of the plane of the film in a small region forming the vortex core pointing either up (p = +1) or down (p = −1) termed as the polarity of the vortex core. Even though the vortex core has a small radius of about 5 - 10 nm [39,40], it plays an important role in the spin dynamics of such structures and consequently has been intensively studied in the last decade.

The vortex element has four energetically equivalent ground states (Fig. 2.4), corresponding to counter-clock-wise (CCW) or clockwise (CW) chiralities and up or down polarities. These vortex states are highly stable against thermal fluctuations. A high static magnetic field of about 0.5 Tesla is required to reverse the core polarity. Additionally, due to the dipole free configuration, these structures prevent cross talk among the adjacent vortices and thus have high magnetic stability and can be placed

closer to each other. These characteristics make magnetic vortices a possible candidate for more stable and high density magnetic data storage devices [41,42]. However, if the magnetic vortex is used in technology, it is necessary to find a way to overcome enormous stability in order to control all four states independently and detect them electrically [41,44]. The magnetic vortex represents a variety of phenomena, such as interacting with magnetic fields, electric currents, temperature gradients, samples surfaces and defects. Understanding and controlling vortex dynamics on the mesoscopic scale can enable the discovery of basic physical processes as well as electronic devices based on control of vortex dynamics.

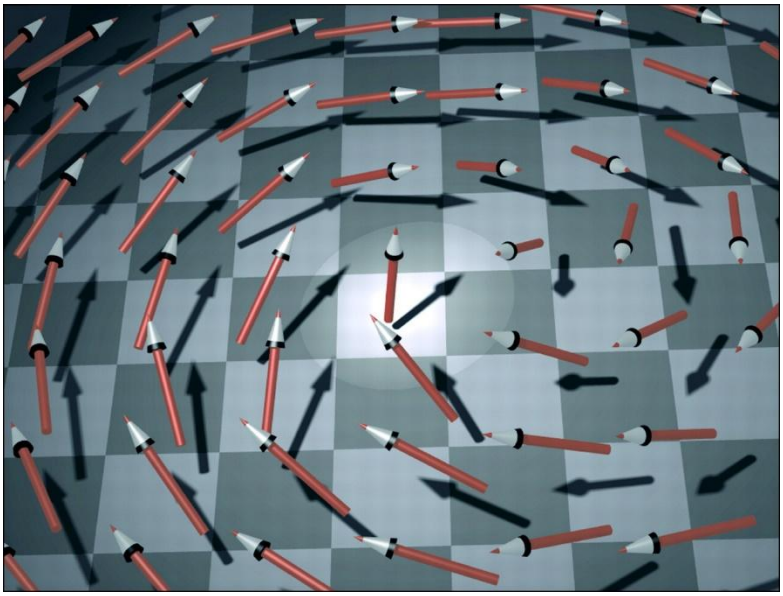

Fig. 2.2 Schematics of magnetic vortex, adopted from [37].

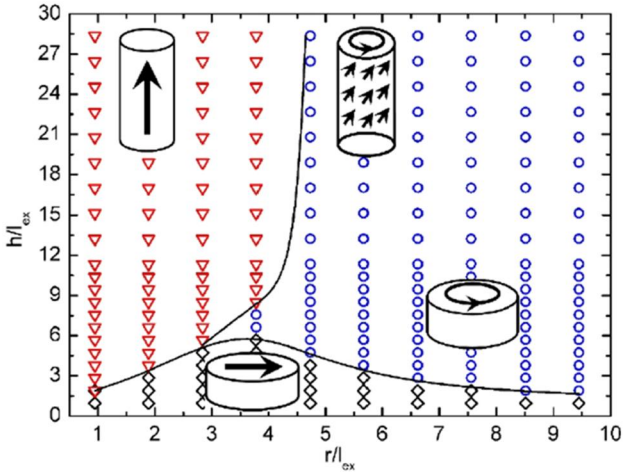

Fig. 2.3 Phase diagram of magnetic configurations for soft magnetic nanodots, adopte from [43].

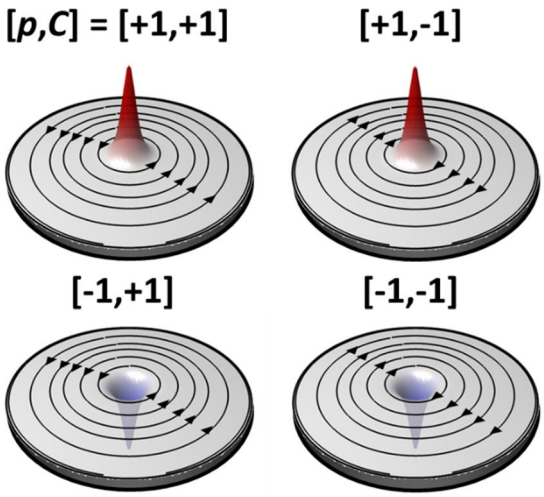

Fig. 2.4 The four degenerate magnetic ground states exist in magnetic vortices.

2.2.1. Vortex core gyration

The magnetic vortex in submicron-size patterned ferromagnetic elements has a rich frequency spectrum of spin excitation, which includes a low frequency mode associated with the translational mode of a vortex core, usually called gyration mode, and high frequency spin wave modes. Starting from the LLG equation (2.1.1), A. A. Thiele [44] derived an equation describing the dynamics of magnetic bubbles as rigid quasiparticles. The Thiele equation was adopted by Huber [47] to the vortex system, and further effects of spin transfer torque [48,49] was introduced.

Thiele assumed a magnetic domain at steady-state motion and transformed the LLG equation into the force balance equation of a magnetic solitary structure, where each term is determined by the initial magnetic configuration and the position vector of the magnetic soliton. With assumption that magnetization distributions are independent along the thickness, the general form of Thiele's equation is

$$-\mathbf{G}\times\dot{\mathbf{X}}+\partial W/\partial\mathbf{X}-D\dot{\mathbf{X}}=0 \quad (2.2.1)$$

where $\mathbf{X}$ is the position vector of vortex core, $W(\mathbf{X})$ is the potential energy of the vortex core shifted from its equilibrium position ($\mathbf{X}$ = 0), $\mathbf{G}$ is the gyrovector, and D is the damping tensor. The gyrovector $\mathbf{G}$ is given by $\mathbf{G}=p|G|$ with $G=-2\pi qM_sL/\gamma$. q is vorticity (topological charge), it determines the direction of the in-plane magnetization components, the L is thickness of the vortex nanodisk, and the γ is gyromagnetic ratio. The damping tensor D is given by $D=-\alpha\pi M_sL/\gamma\left(2+\ln R/R_c\right)$ with some

approximations. The α is damping constant, the R is radius of the vortex nanodisk, the R_c is radius of the vortex core.

The potential energy $W(\mathbf{X})$ can be expressed as

$$W(\mathbf{X}) = W_{exch}(\mathbf{X}) + W_{demag}(\mathbf{X}) = W_0 + \frac{1}{2}\kappa\mathbf{X}^2 . \quad (2.2.2)$$

This potential energy makes the vortex core acting like harmonic oscillator. The potential energy can be described as $\frac{1}{2}\kappa\mathbf{X}^2 = \frac{1}{2}\kappa_x X^2 + \frac{1}{2}\kappa_y Y^2$. The velocity of the vortex core $\dot{\mathbf{X}}$ can be expressed by the angular frequency vector and vortex core position as $\dot{\mathbf{X}} = \omega \times \mathbf{X}$. Inserting this representation form of the vortex core velocity $\dot{\mathbf{X}}$ into the equation (2.2.1), the equation (2.2.1) can be reformulated as

$$-|\mathbf{G}|\omega\mathbf{X} + \kappa\mathbf{X} - D\omega\mathbf{X} = 0 . \quad (2.2.3)$$

Through the equation (2.2.3), we can calculate the frequency of the vortex core gyrotropic motion, as

$$\omega = \frac{\kappa}{|\mathbf{G}| + D} . \quad (2.2.4)$$

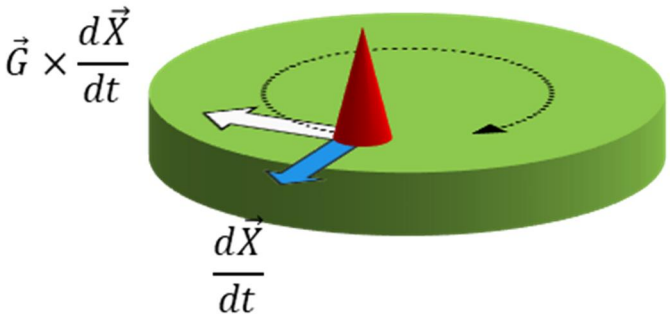

Fig. 2.5 Driving forces acting on the vortex core in the gyration mode.

2.2.2. Vortex core switching

The polarity of the vortex core can be switched by a strong [50-52] external static magnetic field acting in the opposite direction to the vortex core polarization, but the actual device cannot withstand such strong fields. This stability has the advantage that this type of magnetic storage can be stable against interfering magnetic fields, but also turns into disadvantageously because it is more difficult to process data by switching the vortex core. Technological applications need to switch the magnetization states to a much faster and more energy efficient way. A mechanism called dynamic reversal of vortex core has been found to be a noble solution that makes it easier to switch the vortex core polarity [53-55]. Previous studies have shown that instead of an out-of-plane static field, only a few Oe in-plane oscillating magnetic field with a frequency close to the resonant frequency of the vortex core's gyrotropic mode is sufficient to push the vortex core out of its equilibrium position and eventually switch the vortex core polarity on nanosecond scale [56-58].

2.2.3. Interaction between magnetic vortices

The stray field of nearby magnetic vortices can have a significant effect on the static magnetization configuration and the magnetization dynamics [59-61]. It has been observed that vortex gyration can be induced by dipolar interaction between physically separated disks. Dipolar-coupled vortex dynamics has been studied through the theoretical studies, micromagnetic simulation, and experiments [22,23, 62-74].

Shibata et al. theoretically calculated the collective modes and the eigenfrequencies of

vortex core's gyrotropic motion in laterally two coupled magnetic disks [22]. In the rigid vortex model, the interaction energy between two magnetic disks comes from the interaction between surface charges:

$$W_{\text{int}} = C_1 C_2 \left(\eta_{\parallel} X_1 X_2 - \eta_{\perp} Y_1 Y_2 \right) \quad (2.2.5)$$

where $\eta_{\parallel}$, $\eta_{\perp}$ represent the interaction strength.

Recently, some experimental evidences for dipolar coupled vortex dynamics were revealed through various experimental techniques, e.g., X-ray imaging technique [66-70, 75], VNA-ferromagnetic resonance measurements [67], and electrical measurements [71, 76]. This robust mechanism for energy transfer via coupled vortex gyrotropic motion is expected to provide the advantages of fast, tunable energy transfer rate, and low-power consumption. As a mean of manipulating the vortex-based signal transfer, 1D and 2D arrays of ferromagnetic disks with vortex states has also been proposed [77,78].

2.3. Experimental methods

2.3.1. Photo lithography

The fundamental of various processes used to fabricate integrated circuits is the lithography, i.e., the formation of three-dimensional images on the substrate. Photo lithography involves a complex photographic process in which electromagnetic waves are incident on a photoresist which dynamically changes during illumination and forms a 3D relief image on the substrate after development in a suitable chemical called developer. The final resist pattern consists of the substrate covered and uncovered with resist. This pattern is needed for pattern transfer by several mechanisms e.g. etching, ion implantation, deposition and lift-off technique. A single iteration of lithography is a sequential combination of several steps [79].

2.3.2. Electron beam lithography

The basic idea behind electron beam lithography is identical to photo lithography. The substrate is covered with an electron sensitive thin layer of resist which is chemically changed under exposure to the electron beam. A beam of highly focused electrons is scanned in a well-defined pattern across the surface, thus depositing energy in the desired pattern in the resist film to modify the solubility of a resist during a subsequent development step. The exposed structure can be developed in proper chemicals so that the exposed or non-exposed areas can be dissolved in a specific solvent. The main attributes of this technique are the very high resolution and the extraordinary flexibility which can

be applied to a broad variety of materials and an almost infinite number of patterns.

2.3.3. Anisotropic magnetoresistance

The resistance of a ferromagnetic sample depends on the angle between the magnetization and the direction of the current [80-84]. In 1936, N. Mott first reported that the current in the investigated transition metals is mainly carried by *s* electrons, and the electrical resistance is attributed to scattering due to spin-dependent interband *sd* transitions [85]. Non-rotational symmetric charge distributions which are linked to the magnetization direction lead to an anisotropic scattering cross section and thus yield a difference in the resistivity depending on the alignment of magnetization and current [84]. For any angle between the magnetization and the current, the resistivity is given by

$$\rho(\theta) = \rho_{\square} - \Delta\rho \sin^2(\theta) \quad (2.3.1)$$

The resistivity rises to maximum for parallel alignment and fall to minimum for perpendicular alignment. Anisotropic magnetoresistance (AMR) effect is exploited to detect the dynamics of magnetic vortices in this thesis, as later studied in detail in chapter 5.

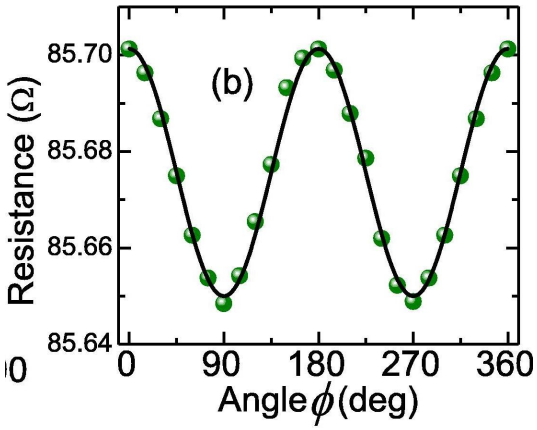

Fig. 2.6 AMR of Py thin film, adopted from [86].

3. Vortex Core Switching by Propagation of a Gyration-Coupled Mode

On the basis of combinations of novel dynamic characteristics in single vortex-state dots and their dipolar-coupled dots, in this part, an efficient alternative to the switching of vortex-core orientations is proposed, which is totally different from earlier-reported magnetic-field- or current-driven vortex-core switching [87-99]. With this switching mechanism, for the first time by micromagnetic simulations, a new-concept RS latch logic operation using vortex-state-dot networks and specific gyration-coupled modes for switching of bi-state vortex-core orientations. A three-magnetic-disk array of magnetostatically coupled vortices is used to demonstrate RS latch logic, one of the most fundamental sequential logic circuits. The output signal of the RS latch depends not only on input signals but also on the already-stored state. While currently existing RS latch logics, consisting of several transistors, are typically volatile, the vortex-network-based RS latch is non-volatile, of unlimited endurance, and low-power-consumptive when using a low-damping material and resonant excitations of specific coupled modes.

3.1. Micromagnetic simulation conditions

To conduct the micromagnetic simulations, we used a model system of three Permalloy (Py: $Ni_{81}Fe_{19}$) cylindrical dots of diameter D = 303 nm, thickness t = 30 nm, and edge-to-edge interdistance D_{int} = 3 nm, as shown in Fig. 3.1. In the model, two different vortex-state configurations were used: type I, all upward core magnetizations in the three disks

along with CCW in-plane curling magnetizations, and type II, upward core magnetization in both end disks and downward core magnetization in the middle disk with the same CCW in-plane curling magnetizations. The Py material parameters were as follows: saturation magnetization $M_S = 8.6\times10^5$ A / m , exchange stiffness constant $A_{ex} = 1.3\times10^{-11}$ J / m , Gilbert damping constant $\alpha = 0.01$ (0.0001 for better resolution), gyromagnetic ratio $\gamma = 2.21\times10^5$ m / A·s , and zero magnetocrystalline anisotropy. The cell size is $3\times3\times30$ nm^3.

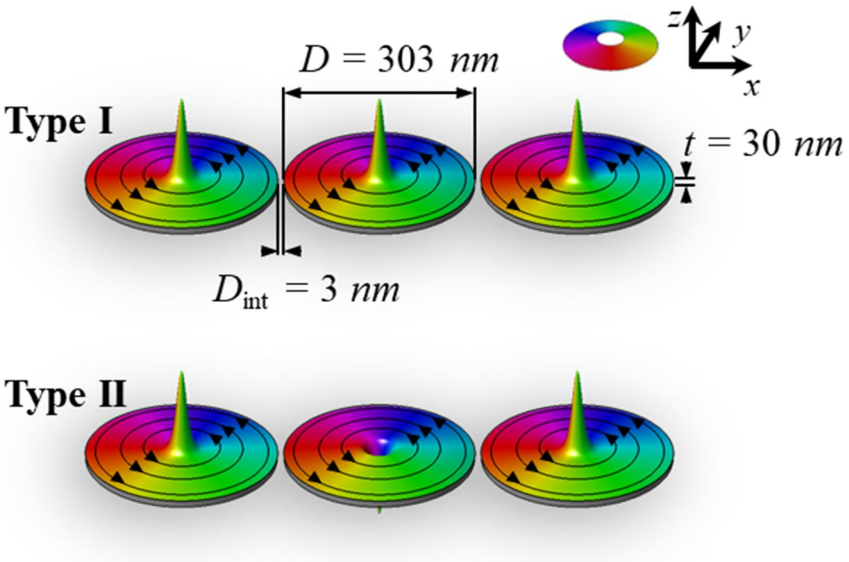

Fig. 3.1 Physically separated Py disks for two different vortex-state configuration types: Type I, three upward cores, Type II, downward core in middle and upward cores in both ends.

3.2. Coupled modes of gyration for the two types of vortex-state configurations

First of all, to excite all of the possible coupled modes of gyration for the two vortex-state configurations (types I and II), the core positioned initially at the center of the left disk (disk 1) was displaced in the +*y* direction by application, only to this disk, of a static local magnetic field in the +*x* direction. After turning off the magnetic field, the position of a single core in each disk was monitored according to the guiding center of each core, $R = (X, Y)$, where

$$X = \int xqdxdy / \int qdxdy$$

$$Y = \int yqdxdy / \int qdxdy \quad (3.2.1)$$

with the topological charge density [100],

$$q = (1/4\pi)\boldsymbol{m} \cdot (\partial_x \boldsymbol{m} \times \partial_y \boldsymbol{m}) . \quad (3.2.2)$$

Then, using the Fast Fourier Transformations (FFTs) of the temporal oscillations of the X component of $R = (X, Y)$ in each disk for 1000 ns, we extracted, for the two configurations, a frequency spectrum from each of the three disks. The three disks showed contrasting FFT power spectra, as indicated in Fig. 3.2. In each disk, two or three distinct peaks were observed in the frequency domain. Since those peaks were rather broadened owing to a certain value of $\alpha = 0.01$ used in the simulation, we also obtained corresponding FFT power spectra (red lines) for the same model but with a lower damping constant, $\alpha = 0.0001$. The individual peaks were denoted as $\omega_i / 2\pi$, with *i* = I, II and III corresponding to 661, 771, and 811 MHz, respectively, for type I, and 604, 771, and 889 MHz, respectively, for type II. Each mode showed the same resonant

frequency for all of the disks. Interestingly, the resonance peak of the second coupled mode (mode II) disappeared in the middle disk for both vortex-state configurations types I and II. Overall, the contrasting heights among the three different mode-peaks as well as among the different disks were ascribed to the corresponding coupled-mode characteristics in the three-disk network.

In order to better clarify the existing coupled modes from the contrasting frequency spectra, we extracted the spatial correlations between the core motions of the individual disks from the inverse FFTs (with 1 MHz window) of all of the peaks of each coupled mode for the three different disks, as shown in Fig. 4.3. The trajectories of the orbiting cores (red-color circles) in the individual disks along with the profiles of the Y components of the core positions represent characteristic standing wave forms of certain wavelengths as expressed by

$$k = m \cdot \pi / 4(D + D_{\text{int}}) \quad (3.2.3)$$

where m =1, 2, and 3 indicative of coupled modes I, II, and III, respectively. [101] In general, for coupled mode I, the three cores are in-phase in their motions; for mode II, the core in the middle acts as a node (i.e., no core motion) while the core motions in both end disks are out-of-phase with each other; for mode III, the core motions between next-neighboring disks are always out-of-phase. For the vortex configurations of type I and type II, the standing wave forms are the same, but the resonant frequencies of modes I and III are different, as indicated in Fig. 3.3. The difference of resonant frequencies of modes I and III can be explained by comparison of the energy of each mode. As seen in Fig. 3.4., in the mode I, the average dipolar energy between disks of type I is higher than

type II. In the contrary, in the mode III, the average dipolar energy between disks of type I is lower than type II.

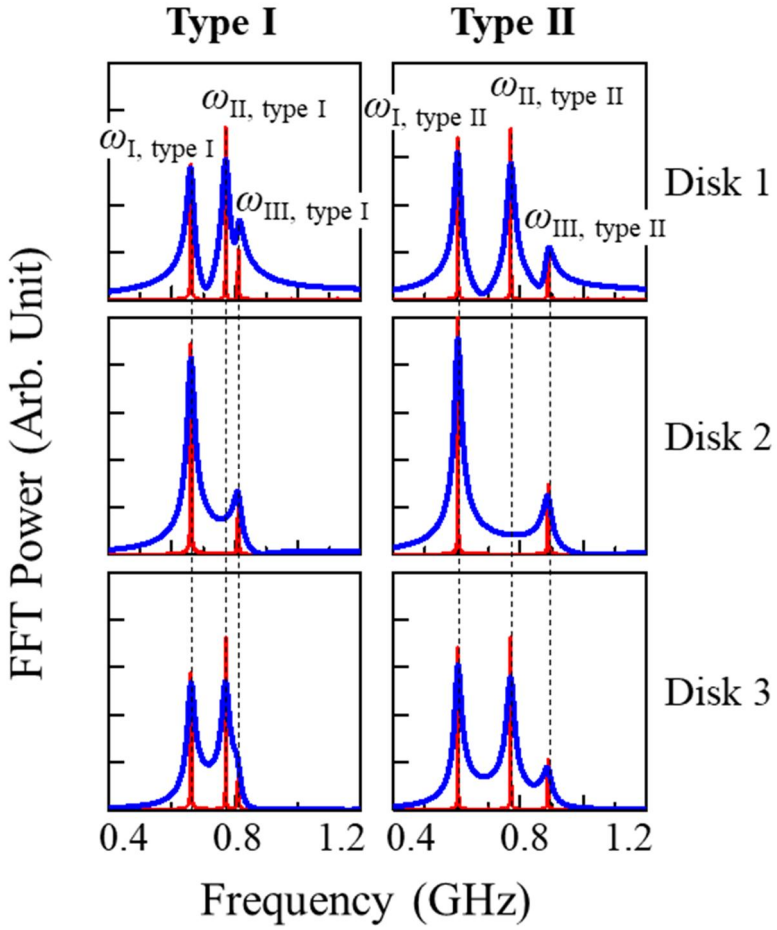

Fig. 3.2 FFTs of oscillatory *x* components of vortex-core position R in each of three disks for Type I and II configurations. The solid blue and red lines are the simulation results obtained for the damping constants $\alpha = 0.01$ and 0.0001, respectively.

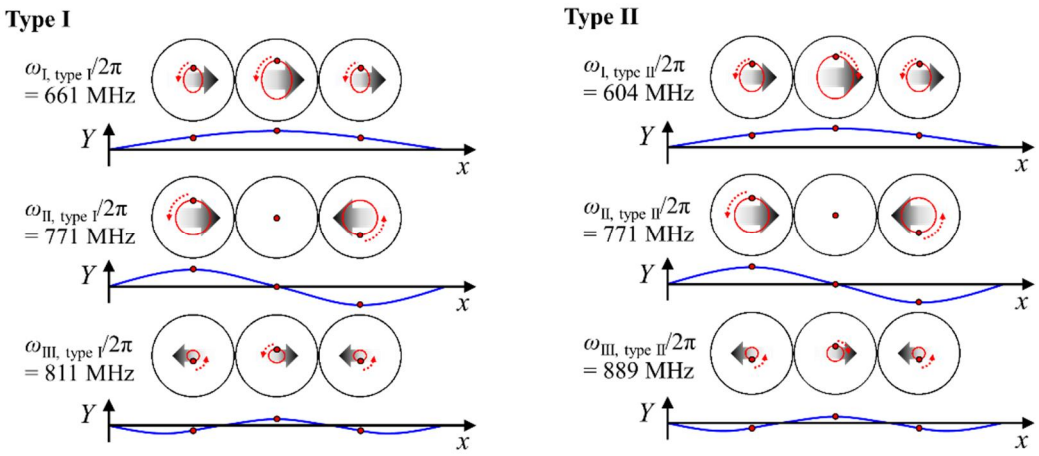

Fig. 3.3 Spatial distributions of core positions in individual disks for indicated coupled modes for both type I and II configurations, as obtained from the simulation results with $\alpha = 0.0001$.

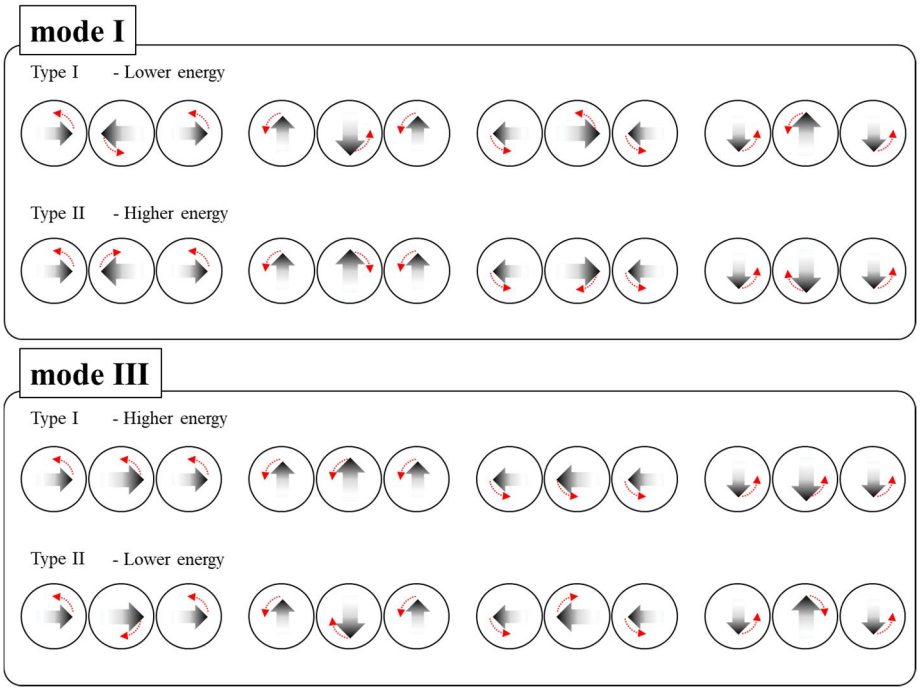

Fig. 3.4 Effective in-plane net magnetizations of a given disks in a unit time of period of $2\pi/\omega$. Dynamic dipolar energy between each mode of type I and II configurations can be compared by relative directions of in-plane net magnetizations in each disk.

3.3. Concept design of reset-set latch device

It was reported that vortex-gyration-coupled modes in a vortex-state coupled network can be used as an information carrier, such as one comprised of vortex-state disk chains. [65, 68] In this regard, we propose herein, for the first time, that a specific coupled mode can be used as a signal to resonantly excite vortex gyration and stimulate core switching. On the basis of coupled mode I's characteristics for both vortex-state configurations of type I and II, the vortex core of the middle disk can be switchable when coupled mode I is excited with a sufficient field strength. The mechanism is as follows. Only the coupled mode I shows that the core orbiting radius in the middle disk is larger than those in both end disks, while the coupled mode II shows almost no gyration in the middle disk, and the coupled mode III shows similar amplitudes of core orbiting radius for the three disks. It is known [102] that the core magnetization is reversed (switched) when the core velocity is greater than the critical velocity required for its core switching. Until now, vortex-core-switching events have been achieved by applications of polarized currents or oscillating magnetic fields that are directly applied to the disk in which a vortex core is desired to be reversed [87-99]. Here we report an alternative way: vortex-core switchability by propagation of a specific gyration-coupled mode (here mode I) transferred from the neighboring disks. Through coupled modes II and III, vortex-core switching in the middle disk cannot be achieved, because the core orbiting radius (core velocity) in the middle disk is not sufficient to reach its critical orbiting radius (critical core velocity). Thus, by application of AC magnetic fields to both end disks for both the type I and II configurations, the excitation of only coupled mode I is sufficient to switch

the vortex-core magnetization of the middle disk. We note that the resonant frequencies of coupled mode I for types I and II are contrasting, 661 and 604 MHz respectively, for a given system.

In order to directly confirm such a switching event in the middle disk by gyration–mode signals transferred from both end disks, we designed a three-vortex-state-disk device with two metallic electrodes positioned only at both end disks (see Fig. 3.5(a)). As input signals, we used AC magnetic fields $\mathbf{H} = H_0 \sin(\omega_{\mathrm{H}} t)\hat{\mathbf{x}}$ with a specific angular frequency $\omega_{\mathrm{H}} = \omega_{\mathrm{I}}$ and a sufficient field strength H_0 (or pulse fields) to excite the gyrations of the vortex cores in both end disks, which gyration can be transferred to the middle disk in coupled mode I. We conducted further micromagnetic simulations using the proposed device (see Fig. 3.5(a)). We first applied a sinusoidal field $\mathbf{H} = H_0 \sin(\omega_{\mathrm{H}} t)\hat{\mathbf{x}}$ simultaneously to disks 1 and 3 with H_0 = 2.5 mT and $\omega_{\mathrm{H}} = \omega_{\mathrm{I,\ type\ I}} = 2\pi \times 661$ MHz for type I and $\omega_{\mathrm{H}} = \omega_{\mathrm{I,\ type\ II}} = 2\pi \times 604$ MHz for type II.

Fig 3.5 (b) shows the characteristic core motions represented by the core velocities during their gyrations excited with ω_{I}, ω_{II} and ω_{III} resonant frequencies for the two initial vortex-core configurations type I and type II. Only for excitation using $\omega_{\mathrm{H}} = \omega_{\mathrm{I}}$ and H_0 = 2.5 mT, the velocity of the middle disk's core (blue color) reaches the critical velocity, $v_{crit} = 330 \pm 37$ m/s for Py, and then the core-switching event occurs at a certain time: t = 12.4 ns for type I and t = 17.7 ns for type II. Even with excitation of coupled mode I, the gyrations of the vortex cores of both end disks are not sufficiently

excited to reach the critical core velocity with that field strength (here H_0 = 2.5 mT). Once the core in the middle disk is switched from the upward to downward core magnetization for type I and from the downward to upward core magnetization for type II, the resonant frequency of coupled mode I becomes off-resonant frequency; thus, the core velocity slows down. Note that the resonant frequencies of coupled mode I for types I and II are sufficiently different, i.e., 661 versus 604 MHz, as already mentioned. In contrast to the resonant excitation of coupled mode I, the other coupled modes' excitations do not lead to any core switching in the middle disk, because a weak excitation of gyration motion cannot stimulate its core to reach the critical core velocity, as shown in the middle and bottom of Fig. 3.5 (b).

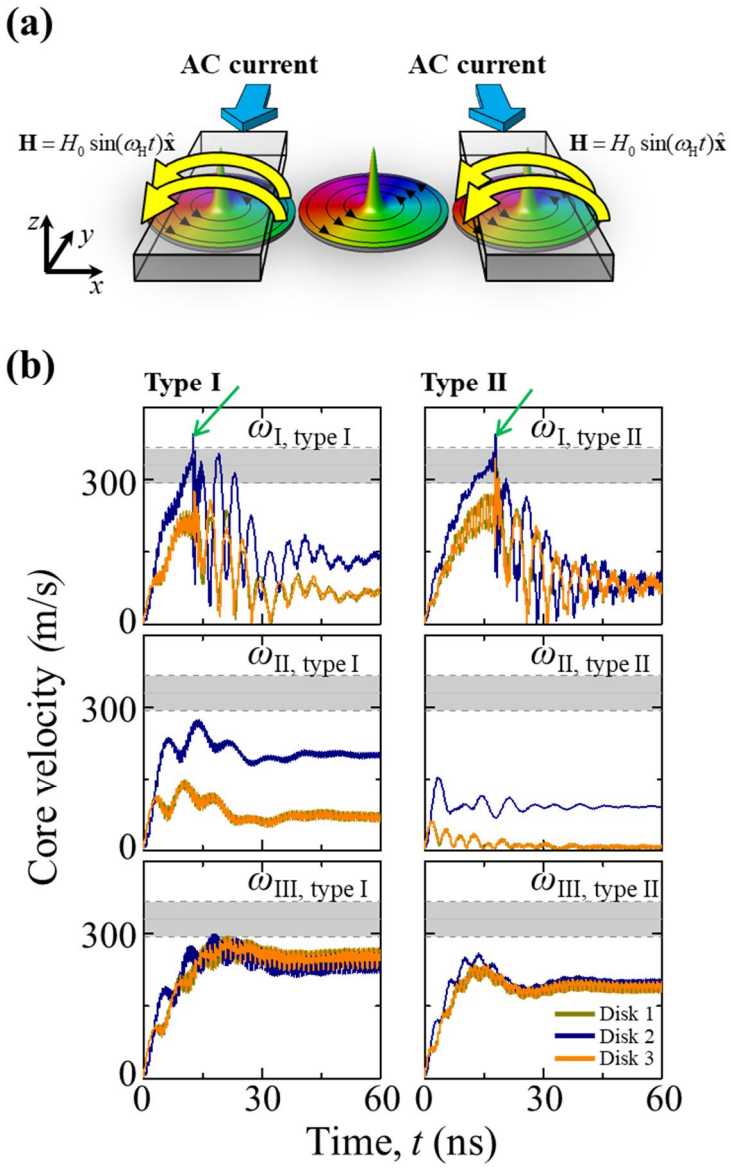

Fig. 3.5 (a) Schematic illustration of RS latch device concept using three coupled vortex-state disks. (b) Vortex-core velocities versus time for individual core gyrations excited by in-phase oscillating fields applied simultaneously only to left and right disks using indicated resonant frequencies of three coupled modes.

3.4. Magnitude of oscillating magnetic field and radius of disks dependent switching behavior

We examined the case of the applying oscillating magnetic field with less and more than 2.5mT. As seen in the Fig. 3.6, in case of the H_0=1.0mT, three cores are gyrate as a certain velocity but no switching happened. In case of the H_0=3.0mT, the core in the disk 2 continuously switched since there was no saturation after the switching. The condition that only the core of disk 2 is switched was investigated for the magnitude of the oscillating field and the radius of the disk when they have an equal interdistance. The results are shown in Fig. 3.7. As increasing the radius of disks, the required magnitude of oscillating field for switching decreased and became narrow. It is because of the stiffness coefficient of the vortex core decreases as the radius of disks increases.

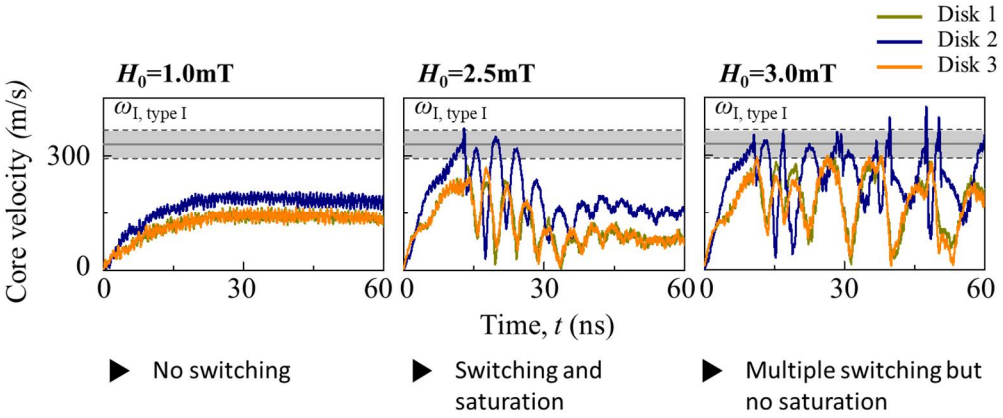

Fig. 3.6 Switching behavior dependence on the field strength, H_0.

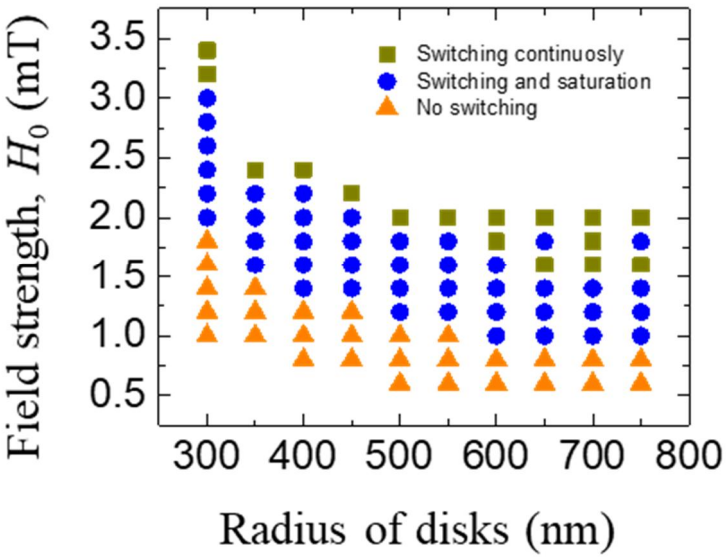

Fig. 3.7 Phase diagram of switching behavior as a function of field strength and radius of disks when they have an equal interdistance D_{int} = 3nm.

3.5. Reset-set latch logic operation

On the basis of the gyration-coupled modes and consequent vortex-core-switching event related to specific coupled-mode signals, we now propose an RS latch logic operation that uses a three-vortex-state-disk array, as shown in Fig. 3.5 (a). The currently existing RS latch is operated based on a bi-stable state for an output. Until any other inputs are applied, the currently set states remain "latched." This logic works by two inputs: "SET" and "RESET," labeled "S," and "R," respectively. The "S" input sets the output Q to "1" while the "R" input resets the Q to "0." The above RS latch operation is well described in Table I. The Q_{prev} is an already set state. When both the S and R inputs are 0, the output Q remains in the previously set state Q_{prev}; when the "S" and "R" inputs are 0 and 1, respectively, the RS latch will be reset. On the other hand, when the S and R inputs are 1 and 0, respectively, the RS latch will be set. When both S and R are 1, the output becomes unpredictable.

In order to directly demonstrate the above-described RS latch operation from micromagnetic simulations, we first defined the input signals S and R as well as the output signal Q: the S = 1 indicates the application of AC fields of $\omega_{\mathrm{H}} = \omega_{\mathrm{I,\,type\,I}} = 2\pi \times 661$ MHz (coupled mode I for type I) with the same phase applied to both end disks; the R = 1 represents the application of AC fields of $\omega_{\mathrm{H}} = \omega_{\mathrm{I,\,type\,II}} = 2\pi \times 604$ MHz (coupled mode I for type II) with the same phase applied to both end disks; both S = 0 and R = 0 represents the null signal. The output Q = 1 corresponds to the downward core magnetization in the middle disk, while Q = 0

corresponds to the upward core magnetization. The Q_{prev} indicates the output state already set before the application of some input signals.

The relations of S, R, Q and Q_{prev} in the latch logic operation, as obtained from further micromagnetic simulations, are shown in Fig. 3.8. By applying the in-phase signal of the resonant frequency of coupled mode I to both end disks (i.e., corresponding to input signals S = 1 and R = 0) for type I, the upward core in the middle disk (i.e., $Q_{prev} = 0$) is switched to downward core magnetization (i.e., Q = 1). By contrast, for type II, the downward core in the middle disk ($Q_{prev} = 1$) is maintained at the same magnetization (Q = 1), because the coupled-mode frequency for type II is different from that for type I. By application of an in-phase AC magnetic field of mode I's resonant frequency for type II, (i.e., corresponding to inputs S = 0 and R = 1) it works the same; that is, the upward core in the middle disk ($Q_{prev} = 0$) does not switch (Q = 0), but the downward core of the middle disk ($Q_{prev} = 1$) for type II is switched to the upward core (Q = 0). Inputting null signals, i.e., S = R = 0, the Q is maintained the same, i.e., $Q = Q_{prev}$. Contrastingly, simultaneous application of in-phase AC magnetic fields of both mode I's resonant frequencies for types I and II (i.e., corresponding to input signals S = 1 and R=1) results in repeatable switching in the middle disk, because the S = 1 input to type I makes the type II configuration and the R = 1 input to type II makes the type I configuration. As a result, the output Q would not be predictable due to such repeatable reversal of the core magnetization in the middle disk. The simulation results exactly correspond to the RS latch operation shown in Table 3.1.

S	R	Q_{prev}	Q	Action
0	0	0	0	Hold state
0	0	1	1	
1	0	0	1	SET
1	0	1	1	
0	1	0	0	RESET
0	1	1	0	
1	1	0	×	Not allowed
1	1	1	×	

Table 3.1 Truth table of RS latch operation

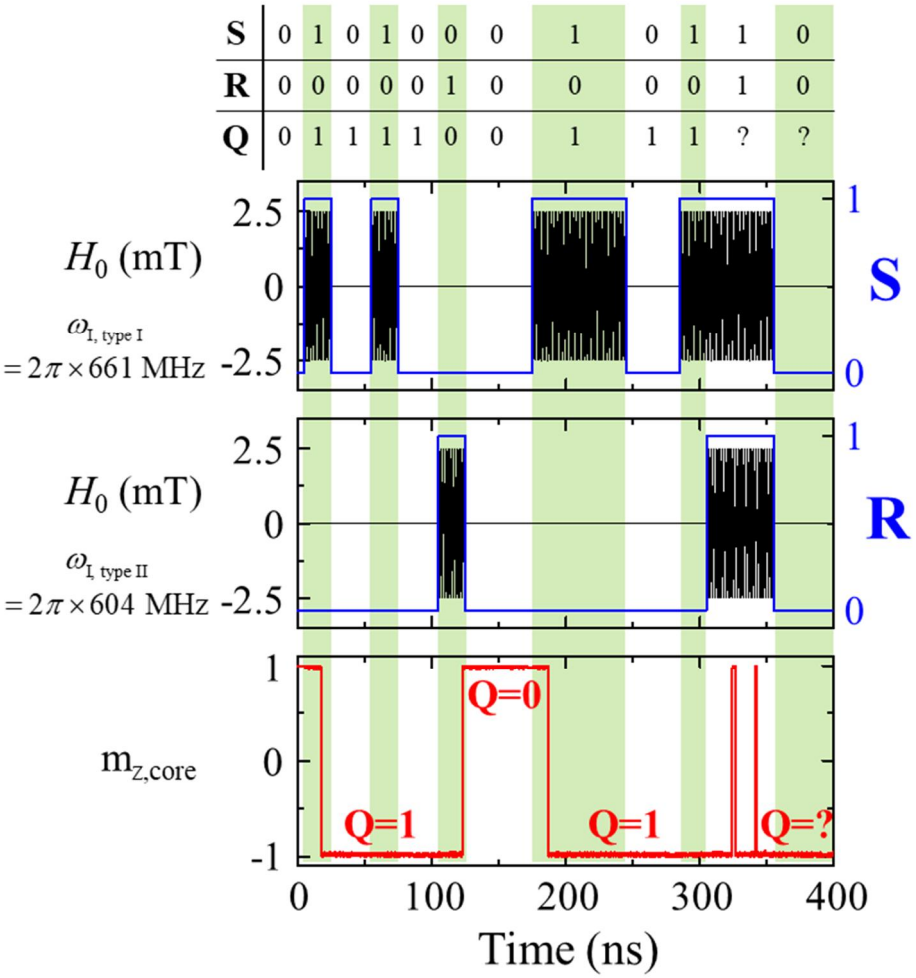

Fig. 3.8 Simulation result for RS latch operation using vortex-state three-disk network. The capital letters “S” and “R” represent setting and resetting, respectively.

4. Control of Gyration Signal Propagation in Coupled Magnetic Vortices

In this chapter, the gyration signal propagation in ferromagnetic disk array is studied. A vortex core undergoing gyrotropic motion exhibits a strongly reduced dynamic stiffness when it is displaced along the flat edge. As a result, the net dynamic core stiffness is also reduced, leading the resonant frequency of vortex core near the flat edge being lower than the resonant frequency for the disk-centered core [103,104]. The resonant frequency can thus either be strongly increased by shifting the core towards the disk's round edge or decreased by shifting the core towards the disk's flat edge. With this tuning mechanism, we demonstrated the method of controlling gyration signal propagation in ferromagnetic disk array which contains circular and chopped disks. Based on this results, we conceptually devised new type of time- and frequency-division demultiplexer device. These results show the large potential of using magnetic vortices and controlled magnetic element's shape for the design of information processing devices and logic gates. These proposed low-damping vortices based demultiplexer devices have enormous tunability by the external magnetic field or the shape of the magnetic elements.

4.1. Dynamics of the single and coupled disk array

As ground work, the bias field and the disk shape dependence of the gyrotropic resonant frequency of the vortex core is studied. To solve the motions of individual magnetizations in the Py disks, we used the mumax3 code that utilizes the Landau-

Lifshitz-Gilbert (LLG) equation $\partial \mathbf{M} / \partial t = -\gamma \mathbf{M} \times \mathrm{H}_{\mathrm{eff}} + (\alpha / M_S)\mathbf{M} \times \partial \mathbf{M} / \partial t$, where $\mathrm{H}_{\mathrm{eff}}$ is the total effective field, M_S is the saturation magnetization, and α is the Gilbert damping constant. The Py material parameters were as follows: saturation magnetization $M_S = 8.0 \times 10^5$ A / m , exchange stiffness constant $A_{ex} = 1.3 \times 10^{-11}$ J / m , Gilbert damping constant $\alpha = 0.01$, gyromagnetic ratio $\gamma = 2.21 \times 10^5$ m / A · s, and zero magnetocrystalline anisotropy. The cell size was 5 × 5 × 40 nm3.

At first, we considered two different shape of single disks, chopped and circular, having diameter *D* = 1000 nm, thickness *t* = 40 nm, and chopped length 150nm, as shown in Fig. 4.1. Magnetic vortices in each disk had upward core and CCW in-plane curling magnetizations. To excite gyrotropic resonant mode for the vortex in the two types of disks, the core positioned initially at the center of the disk was displaced in the +*y* direction by application, only to this disk, of a static local magnetic field in the +*x* direction. After turning off the magnetic field, the net magnetization in disk was monitored. Then, using the Fast Fourier Transformations (FFTs) of the temporal oscillations of the *X* component of net magnetization in the disk for 1000 ns, we extracted gyrotropic resonance frequencies as a function of bias field H_y, as shown in Fig. 4.2. The peaks of the two types of disks were corresponding to 320 MHz, for external field is zero, 352 and 355 MHz respectively, for external field is 15mT to y direction, and 308 and 350 respectively, for external field is -15mT to y direction. The core in the chopped disk moves to the flat edge as the amplitude of bias field decrease. In the circular disk,

frequency becomes higher as the core is displaced from the disk's center due to a core stiffening. In the contrast, as M. Sushruth *et al*. had already reported, in the chopped disk, a core undergoing gyrotropic motion near the flat edge exhibits a strong frequency downshifting because of the reduced dynamic stiffness [104].

On the basis of this anistotropic gyrotropic resonant frequency shifting in the chopped disk, we devised a control method of gyration signal transmission in the disk arrays consisting of chopped disks and circular disks. Our model system is shown in Fig. 4.3. Type I array consists of two circular disks at each end and a chopped disk in the middle, having same size with above single disks, and edge-to-edge interdistance D_{int} = 100nm. To compare with type I array, we also make type II array, which consists of three circular disks. To excite all of the possible coupled modes of gyration for the two vortex-state configurations (types I and II), the core positioned initially at the center of the left disk (disk 1) was displaced in the $+y$ direction by application, only to this disk, of a static local magnetic field in the $+x$ direction. After turning off the magnetic field, the net magnetization of a single core in disk 1 was monitored and Fourier transformed to extract frequency spectra as a function of bias field. The two types of arrays showed FFT power spectra, as indicated in Fig. 4.4. In disk 1, two or three resonant mode were observed. In disk 1, three distinct peaks were observed in the frequency domain. Since the existence of chopped disk in the middle of the type I array, there are only two peaks in the type I array when the external field is -15mT to y direction, while there are three peaks in the type II array. This result means that the vortex-state disks of type I array are not coupled under the -15mT external field.

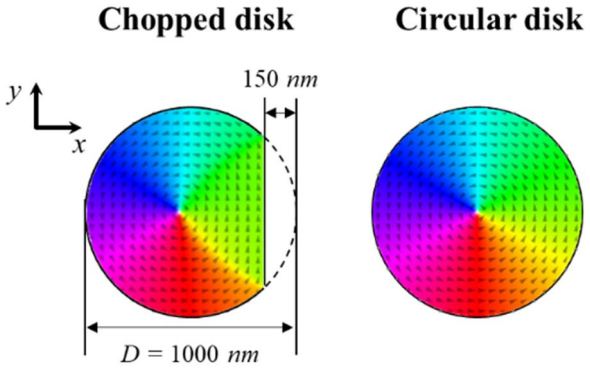

Fig. 4.1 Simulated vortex configurations in isolated chopped disk and circular disk under the zero bias field.

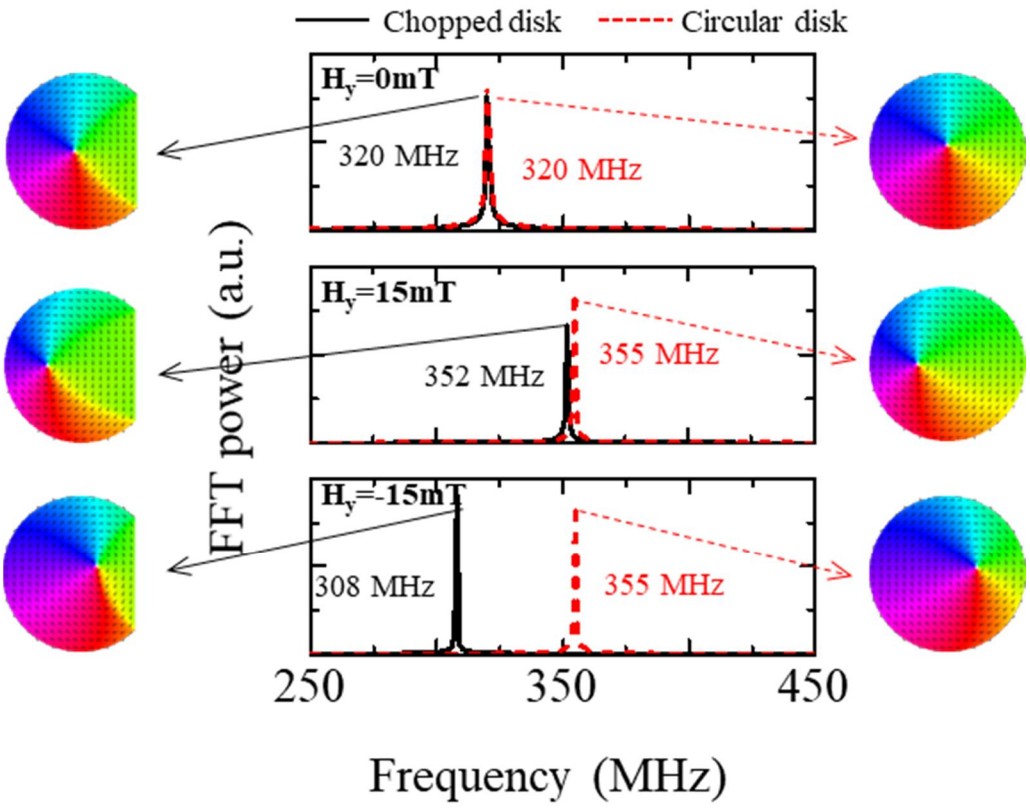

Fig. 4.2 Gyrotropic resonant frequency spectra and vortex configuratoins in isolated chopped disk and circular disk under the three different y-direction bias fields.

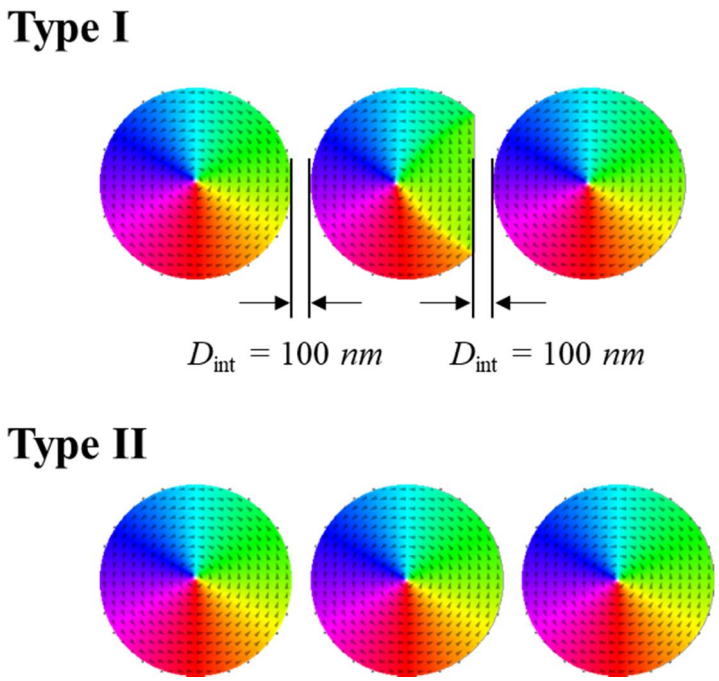

Fig. 4.3 Simulated vortex configurations in the two types of disk arrays under the zero external magnetic field.

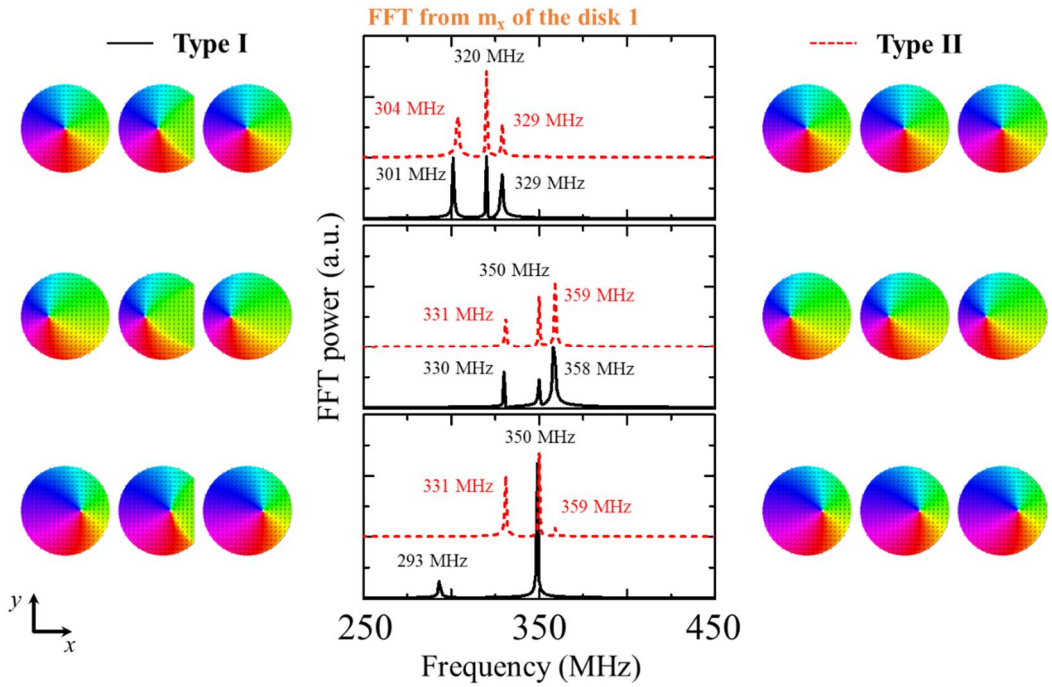

Fig. 4.4 Gyrotropic resonant frequency spectra and vortex configuratoins in the two types of disk arrays under the three different y-direction bias fields.

4.2. Control of gyration signal propagation by in-plane bias field

We have studied the transmission of the gyration signal in type I and type II arrays. Gyration signals are excited by applying sinusoidal field $\mathbf{H} = H_0 \sin(2\pi ft)\hat{\mathbf{x}}$ with H_0 = 0.2mT to disk 1 in both arrays. We used f = 320MHz for H_y = 0mT and f = 350MHz for H_y = ±15mT, which are close to the resonant frequency of single vortex under each bias-field. Fig. 4.6 (a) shows the time resolved gyration signal amplitude (net magnetization, m_x). The gyration signal in the type I array is hindered by disk 2 and did not propagate to the disk 3 under H_y = -15mT, since the core of the chopped disk 2 displaced to flat edge by bias field and the resonant frequency became lower while resonant frequencies of both end disks became higher. In the case of H_y = 0mT and H_y = 15mT, the gyration signals transmitted much better than H_y=-15mT case in the type I array. In the type II array, the gyration signals propagated well in all cases of bias fields H_y = 0mT and H_y = ±15mT.

Gyration signal amplitudes as a function of frequency are shown in Fig. 4.6 (b). The gyration signal in disk 1 have peaks near the coupled modes in both type I and type II arrays under the bias fields. In case of type I under H_y = -15mT, the transmittance of gyration signal was very low near f = 350MHz and only small signal transmitted near f = 290 MHz which is the resonant frequency of the core in the chopped disk under H_y = -15mT. In contrast, in case of type I under H_y = 15mT, the gyration signal propagates well at the frequency range of 330MHz < f < 350MHz. This bias field directional transmission difference makes us to enable to switch “on” and “off” of gyration signal propagation in type I array. At this point, we can expect this method to have enormous tuneabilities through designing the dimension of arrays and varying field strength.

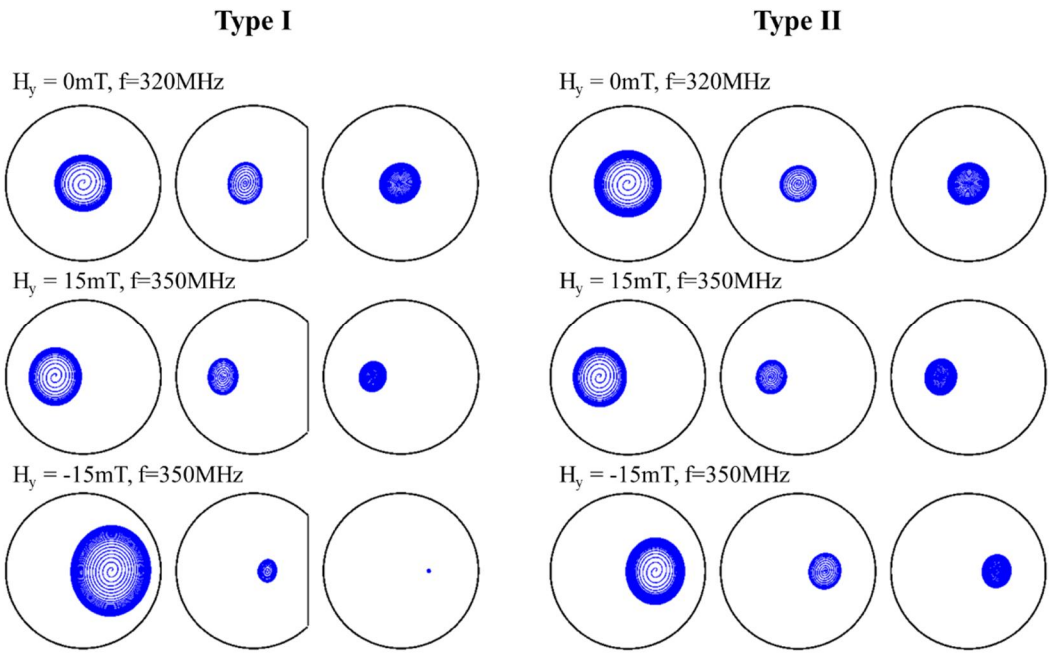

Fig. 4.5 The core motion's trajectories in each disk when sinusoidal field is applied to disk 1, which are magnified 5 times for better illustration.

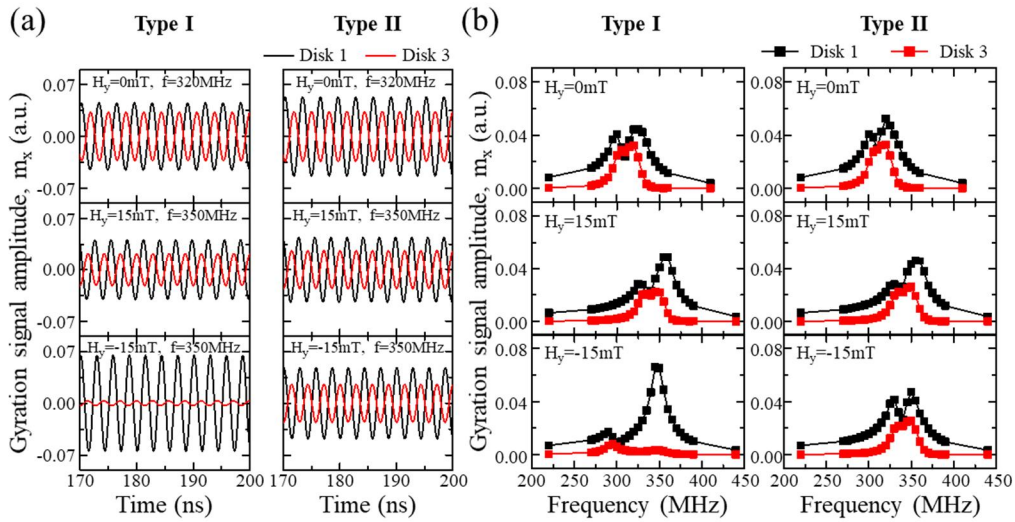

Fig. 4.6 (a) Time resolved gyration signal amplitude (net magnetization, m_x) in the disk 1 and disk 3 of the type I and type II arrays. Gyration signals are excited by applying sinusoidal field $\mathbf{H} = H_0 \sin(2\pi ft)\hat{\mathbf{x}}$ with H_0 = 0.2mT to disk 1. (b) Gyration signal amplitude as a function of frequency f under the three different bias fields.

4.3. Control of gyration signal propagation by vortex core switching

In order to examine the gyration signal propagation in the different polarity configurations, we conducted more simulation for the polarity configurations of (P_1, P_2, P_3) = (1, 1, 1), (1, 1, -1), (1, -1, 1), (-1 , 1, 1). The spectra of gyration signal propagation in type I array are showed in Fig. 4.7, and type II in Fig. 4.8. When external bias field is 15mT to y direction, the gyration signals propagated well to right disk in the all configuration. When external bias field is -15mT to y direction, in the case of (1, 1, 1), (1, 1, -1), (-1, 1, 1), the gyration signals did not propagate to right disk, but in the case of (1, -1, 1), the gyration signal propagate well. In the type II array, the gyration signals propagated well to the right in the all cases.

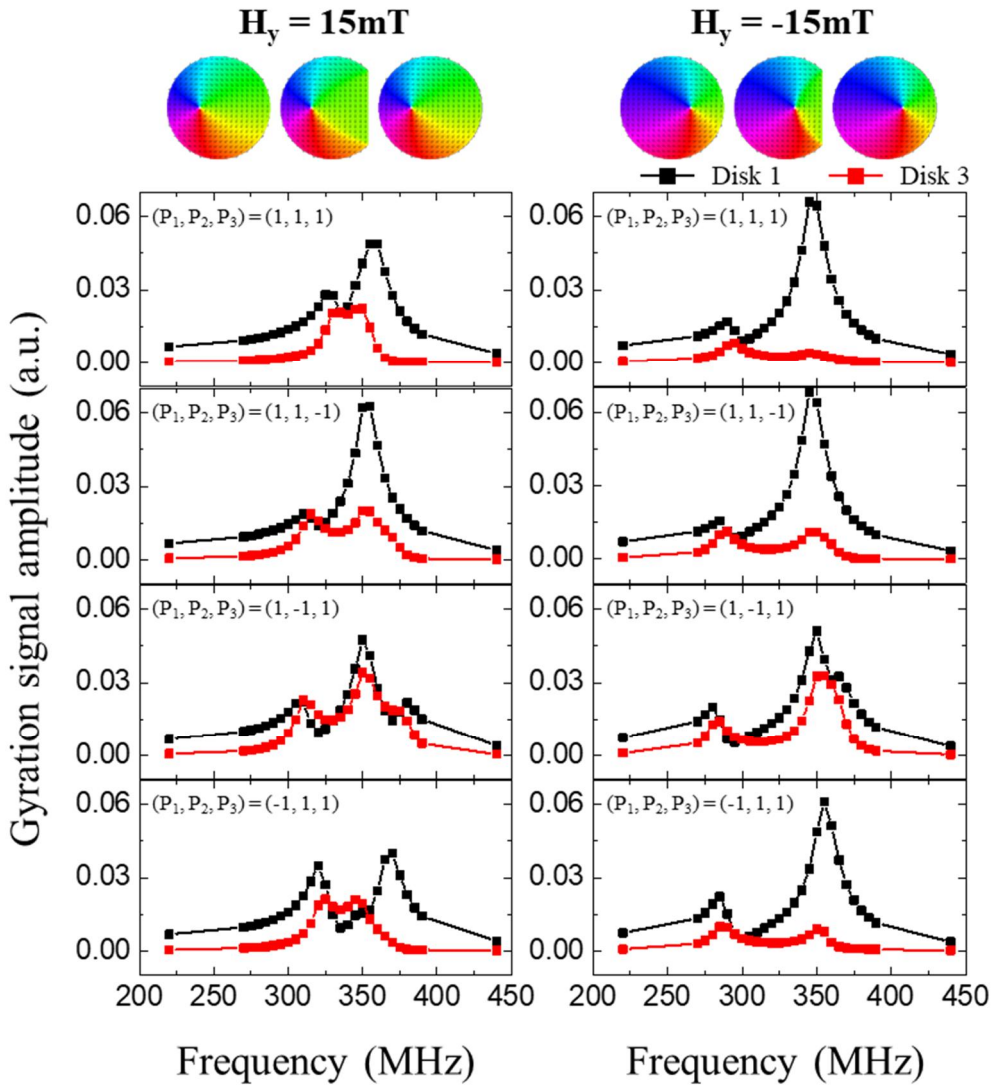

Fig. 4.7 Gyration signal amplitude as a function of frequency in the type I arrays which have polarity configurations of (P1, P2, P3) = (1, 1, 1), (1, 1, -1), (1, -1, 1), (-1, 1, 1) under the 15mT bias field to ±y direction.

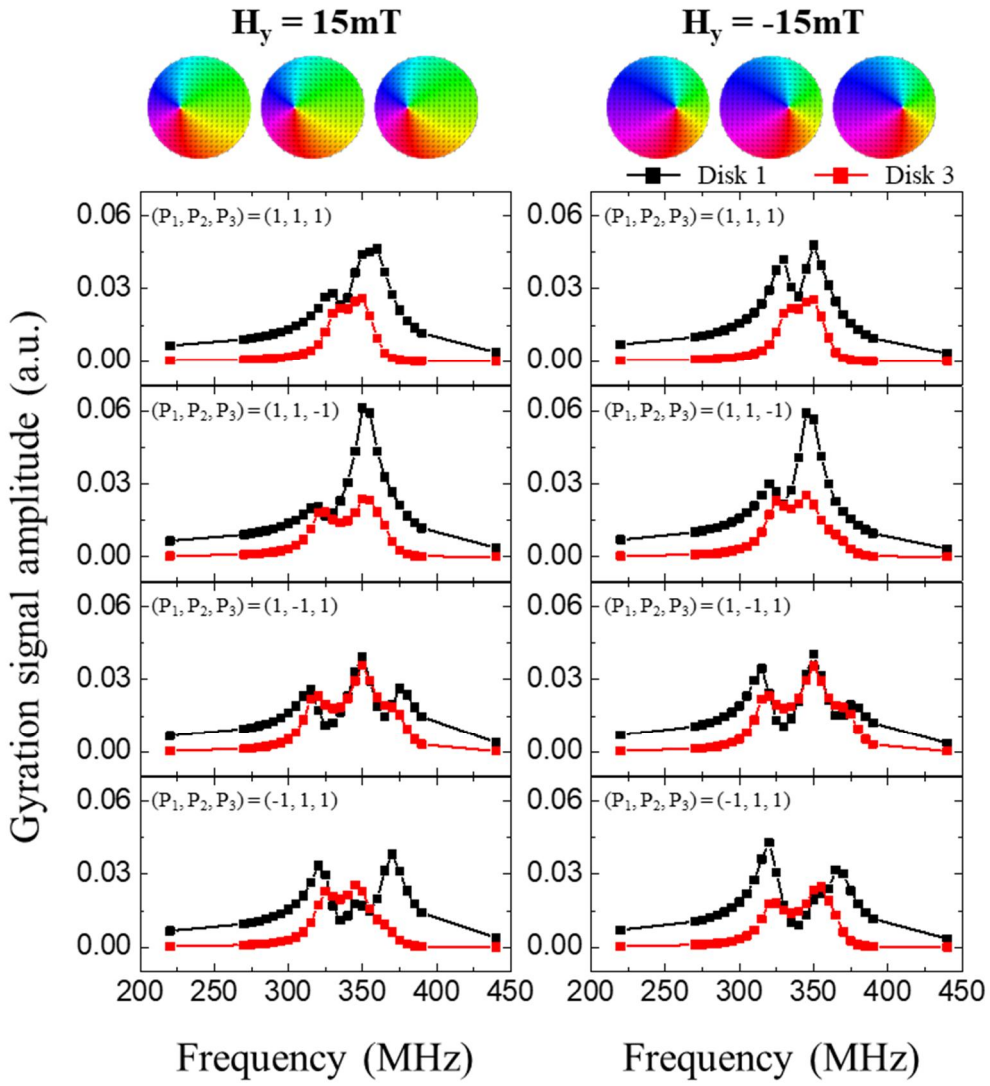

Fig. 4.8 Gyration signal amplitude as a function of frequency in the type II arrays which have polarity configurations of (P1, P2, P3) = (1, 1, 1), (1, 1, -1), (1, -1, 1), (-1, 1, 1) under the 15mT bias field to ±y direction.

In order to understand this uncommon behavior in the case of (1, -1, 1) polarity configuration in the type I array, we observed the stray field while the gyration signal had propagated, as seen in the Fig. 4.9. We could not catch big difference between (1, 1, 1) and (1, -1, 1) polarity configurations, so we differentiated the stray field by time, as seen in the Fig. 4.10.

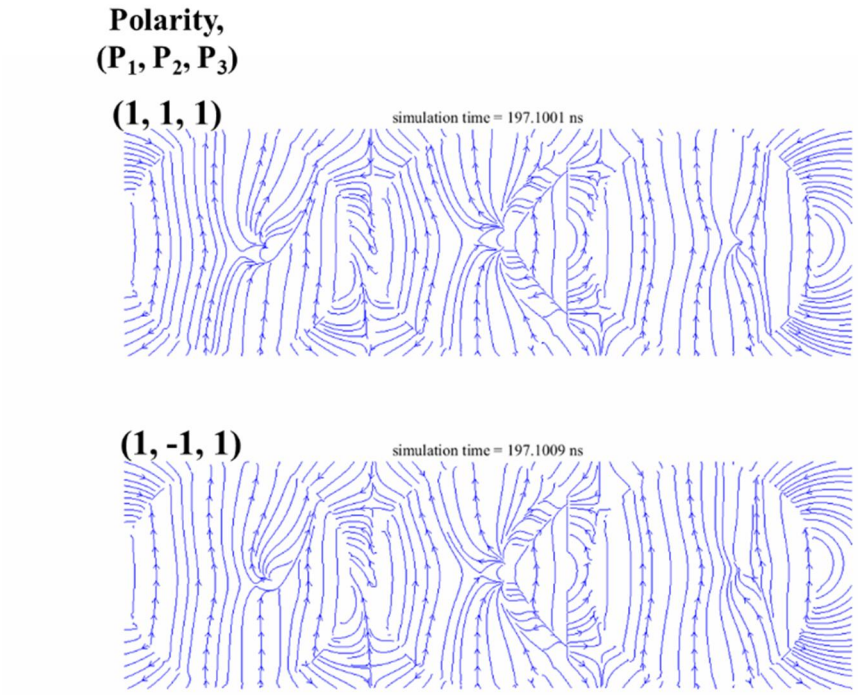

Fig. 4.9 Stray field distribution while the gyration signal propagated from left disk to right in the type I array.

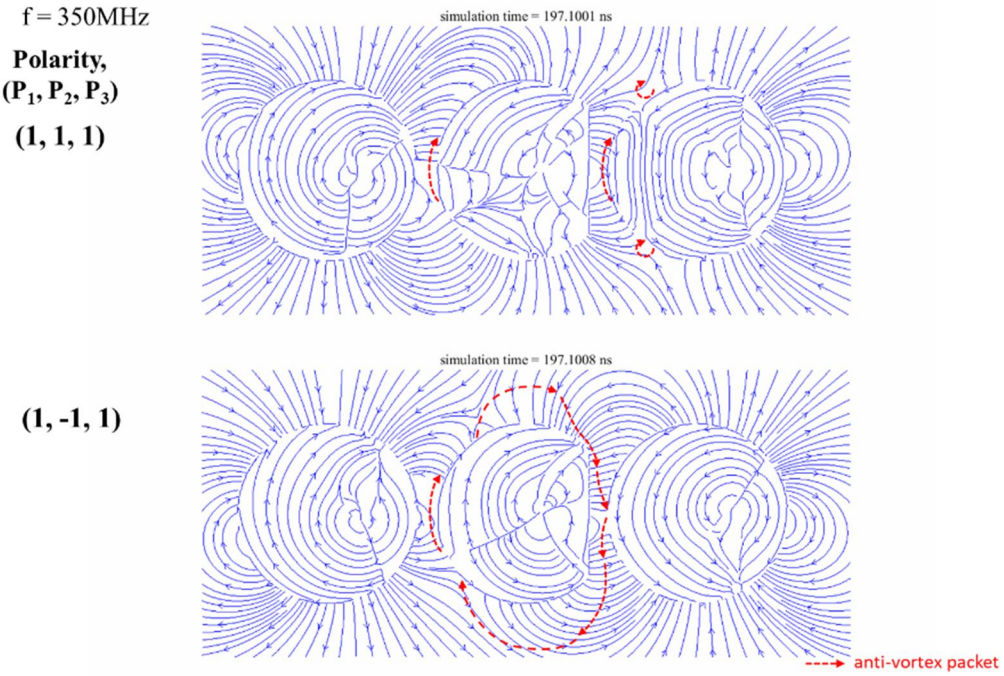

Fig. 4.10 Time derivatives of stray field distribution while the gyration signal propagated from left disk to right in the type I array. Red dotted lines represent the path of anti-vortex packets.

We observed the antivortex packets are moving during the core gyration [105]. This packet collides with other antivortex structures which originate at the boundaries of the disks. The antivortex packets discussed here are no particle in the true sense and their collisions are only a result of the interacting stray fields. This path of antivortex and interactions are shown in Fig. 4.10. There are more collisions in the (1, -1, 1) than (1, 1, 1) polarity configuration. This result makes us possible to switch “on” and “off” of gyration signal of right disk simply by switching the polarity P_2. Vortex core switching can be accomplished with low power consumption by various methods, and the polarity has non-volatility, thus this control method is low power consumptive.

4.4. Concept design of time-division demultiplexer device and its operation

Based on these insights, the design of a time-division demultiplexer prototype device has been developed. The proposed device is shown in Fig. 4.10. We designed the five-vortex-stated disk device with a metallic electrode positioned above the disks. Magnetic vortices in each disk had upward core and CCW in-plane curling magnetizations. The device had chopped disks at the 2nd and 4th, and circular disks at the 1st, 3rd, and 5th of the array. Each cut region of the chopped disks faced outward from the center of the array.

A typical time-division demultiplexer takes one input line and then switches it to any one of a number of individual output lines at a time. In our case, one single input corresponds to sinusoidal field applied to middle disk with frequency range of 335MHz < f < 350MHz, and two outputs corresponds to gyration signal in the both end disks. By switching the direction of dc current I_{dc} applied to the electrode above the disk array, we could select the direction of gyration signal propagation. Gyration signals are excited by applying sinusoidal field $\mathbf{H} = H_0 \sin(2\pi ft)\hat{\mathbf{x}}$ with H_0 = 0.2mT to input. When input=1 and leftward I_{dc} (H_y = -15mT), the core of 2nd disk displaced to round edge and the core of 4th disk displaced to flat edge, thus, gyration signal propagated only to left direction, as shown in Fig. 4.12 (a). In the contrast, when input=1 and rightward I_{dc} (H_y = 15mT), the core of 2nd disk displaced to flat edge and the core of 4th disk displaced to round edge, thus, gyration signal propagated only to left direction, as shown in Fig. 4.12 (b). The gyration signal ratio of output 1 to output 2 when leftward I_{dc} was applied (output 2 to output 1 when rightward I_{dc} was applied) is about 10dB in the frequency range of 330MHz < f < 350MHz. This illustrates the possibility to switch the information channel

in the proposed vortex demultiplexer by means of locally generated Oersted fields. This simulation result exactly corresponds to the demultiplexer operation shown in Table 4.1.

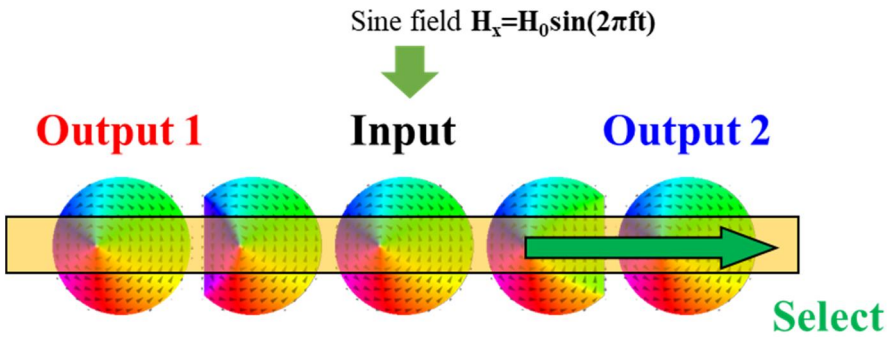

Fig. 4.11 Schematic illustration of demultiplexer device using five coupled vortex-state disks.

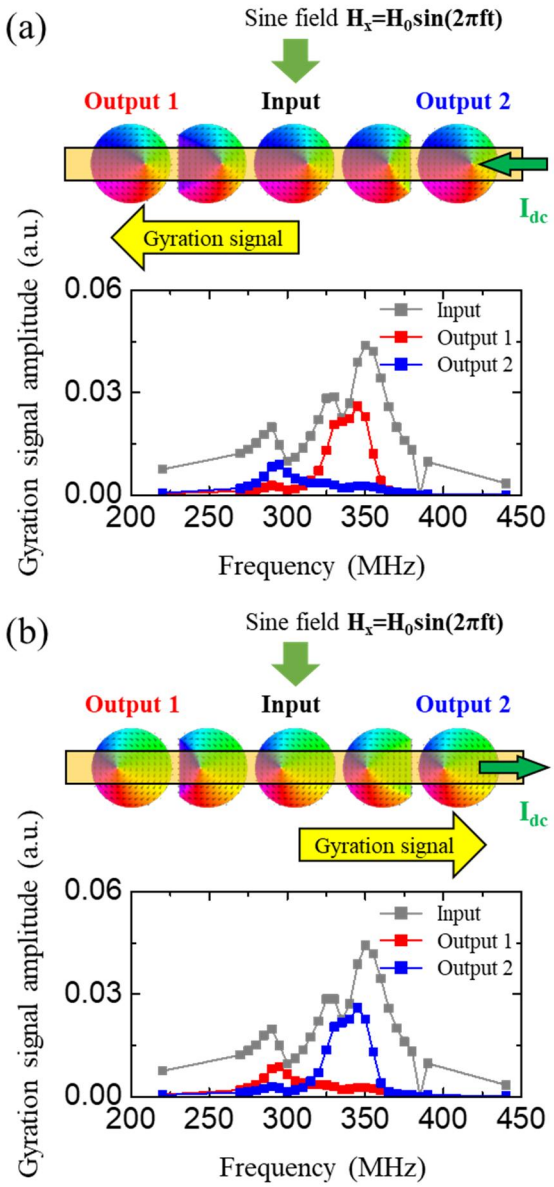

Fig. 4.12 The time-division demultiplexer based on the vortex. Gyration signal excited by applying sinusoidal field to input propagates to (a) output 1 when select=0 (H_y = -15mT) and to (b) output 2 when select=1 (H_y = 15mT) as a function of frequency.

Truth table

Input	Select	Output 1	Output 2
0	0	0	0
0	1	0	0
1	0	1	0
1	1	0	1

Table. 4.1 Truth table of demultiplexer operation.

4.5. Concept design of frequency-division demultiplexer device and its operation

We also proposed the frequency-division demultiplexer device based on the vortex. The proposed device is shown in Fig. 4.13 (a). We designed the five-vortex-stated disk device which had had chopped disks at the 1st and 2nd, and circular disks at the 3rd, 4th, and 5th of the array, with a metallic electrode positioned above the disks. Magnetic vortices in each disk had upward core and CCW in-plane curling magnetizations. Cut regions of the chopped disks faced leftward.

The device was operated under the rightward I_{dc} (H_y = 15mT), which moved the cores in chopped disk along the flat edges. This makes the 1st and 2nd disks a lower frequency f_1 channel, and makes the 4th and 5th disks a higher frequency f_2 channel. To prove this channeling, the gyration signal was excited by applying sinusoidal field $\mathbf{H} = H_0 \sin(2\pi ft)\hat{\mathbf{x}}$ with H_0 = 0.2mT to input and observed the amplitude of gyration signal at outputs in Fig. 4.13 (a). The gyration signal had highest amplitude at f_1 = 290MHz in output 1, and at f_2 = 345MHz in output 2. The gyration signal ratio of output 1 to output 2 was 9.25dB at f_1 and ratio of output 2 to output 1 was 13.4dB at f_2. These operation frequencies can be tuned by adjusting the intensity of the dc current (bias field) or the cut area of chopped disks.

After demonstrating the working principle of the frequency-division demultiplexer device, it was verified that both gyration signals with different frequencies can pass the device simultaneously without disturbing each other, as shown in Fig. 4.13 (b). In addition, it has been verified that the phase of the gyration signals is not changed in case a simultaneous transmission takes place instead of single frequency excitations. This is also

shown in Fig. 4.13 (b) by comparing the phase evolution of the gyration signal amplitudes in the output.

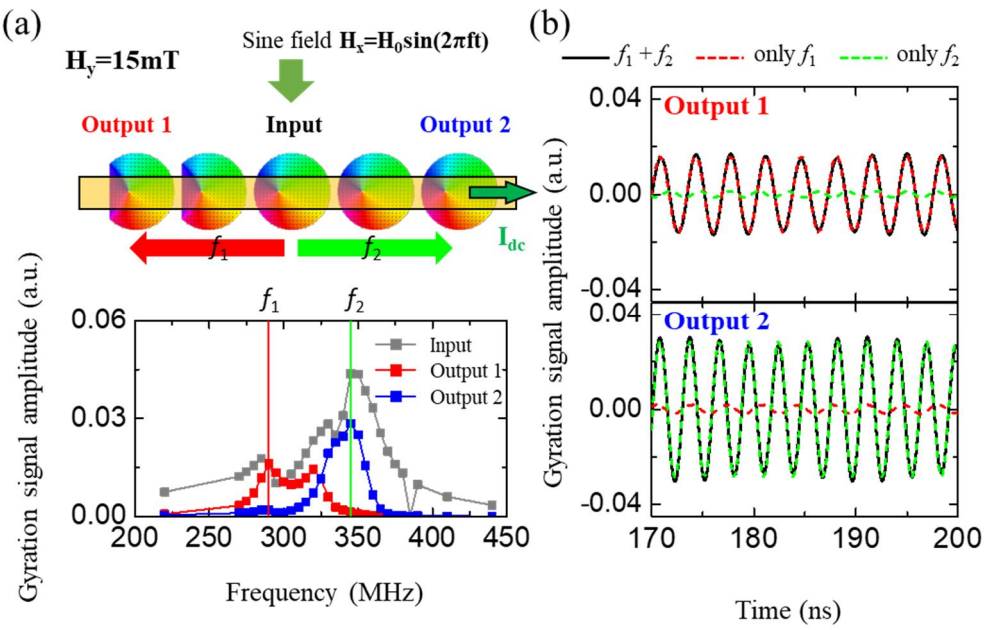

Fig. 4.13 The frequency-division demultiplexer based on the vortex. (a) Gyration signal amplitude in the input and outputs as a function of frequency of applied sinusoidal field under H_y = 15mT. (b) The simultaneous excitation of gyration signal at f_1 and f_2 in the input, the resulting gyration signal amplitude in each output.

5. Electrical Measurement of the Gyrotropic Resonance of a Magnetic Vortex in Circular and Chopped Disks.

The theoretical background of magnetic vortex dynamics and the electrical method of detecting it are illustrated in the introduction. The measurement setups and results obtained from aforementioned methods will be presented throughout this chapter. Two disk samples, chopped and circular, are fabricated for electrical measurement. The DC AMR characteristics of the vortex-state in chopped disk and circular disk are measured. After that, the vortex core's gyrotropic resonant modes are detected by means of rectification measurement. These results are verified by simulation results under the similar conditions.

5.1. Sample fabrication

Samples are fabricated using several steps of the photo lithography, electron-beam lithography and the lift-off processing of positive electron-beam resists onto silicon substrates with a 2000nm silicon-oxide coating.

[Photo lithography]

Substrate preparation: A typical silicon substrate with 2000nm silicon dioxide layer is prepared. The first step is cleaning the substrate, which involves dip in acetone in the sonication bath, dip in iso-propanol and blow dry with N_2 to get rid of dust, debris, contamination or smudges on it.

Resist coating: In the next step the substrate is coated uniformly with photo resist. For our device fabrication, we used a positive photoresist, GXR 601, 46 cps. To coat the resist, the substrate was placed into the spinner on a suitable chuck and a viscous liquid solution of photoresist is dispensed onto the wafer to cover the substrate. The wafer was spun rapidly at 4500rpm for 40s which produce a resist layer of thickness about 2μm. To harden the resist, we baked substrate at 90℃ for 90s with a hot plate.

Exposure: In this step the exposure of the resist through an photo mask is performed. A commonly used mask substrate is transparent borosilicate glass or fused silica because of its lower thermal expansion coefficient and high transmission at lower wavelengths. Lithographic photomasks are typically covered with a pattern defined with a chrome metal absorbing film. The UV-photolithography with a wavelength of 365nm and 500W power was used as the exposure source in our case.

Development and post processing: The next step is the development process. The exposed resist is removed by a suitable developer solution and thus producing a resist pattern. For proper development of the exposed resist, we agitated the wafer in the Az300mif developer for about 60s and then rinsed it with deionized water for 60s to remove the developer from the substrate and to stop further developing process. Thereafter the sample was blown dry with N_2 and inspected under the optical microscope to confirm a proper lithography process.

[E-beam lithography]

Resist coating: To perform electron beam lithography, we need a resist which changes

chemically under the exposure of the electron beam. We used 950K PMMA (polymethyl methacrylate) A4 and 495K PMMA A3. It is the standard positive e-beam resist and remains one of the highest resolution resists available. Spin 495K PMMA A3 over the substrate at 3000 rpm for 40s. Then place the substrate on a hotplate at 170 ℃ for 5 min for evaporation of excess solvent. Repeat the same spin-coating proves with 950K for a bilayer system and bake the sample for 5 min.

Patterning and exposure: The pattern is created directly from a digital representation on computer and the electron beam is scanned in a defined pattern across the substrate. In our system all realizations are based on the CAD layout editor for the structure design. The following parameters are used while exposing our samples during EBL: Accelerating voltage – 100kV, measured beam current – 1nA. The exposure dose depends upon the pattern size and substrate. We used 850 $\mu C/cm^2$.

Development: Methyl-isobuthyl-ketone (MIBK) : IPA = 1 : 1 mixture is used to develop the e-beam resist for 90s in our experiment. Then rinse in pure IPA for 1min to stop the developing process and to avoid removal of e-beam resist from unwanted areas. Then the sample is blown dry with N_2 and inspected under optical microscope.

Deposition and lift-off: After the removal of the exposed resist the desired thickness of the metal is deposited on the substrate. For making the 1000nm diameter Py disk, we used sputtering, and then after one more e-beam lithography patterning, Au electrode is deposited by e-beam evaporator. For a passivation purpose, very thin Ru layer of 2nm is deposited on the Py film.

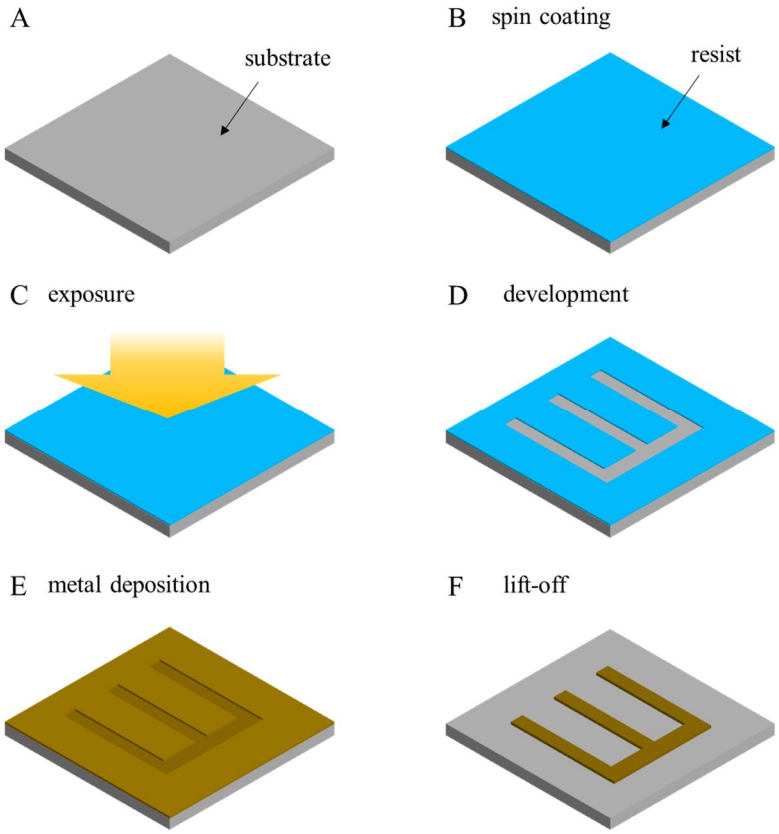

Fig. 5.1 Schematic illustration of lithography and lift-off processing

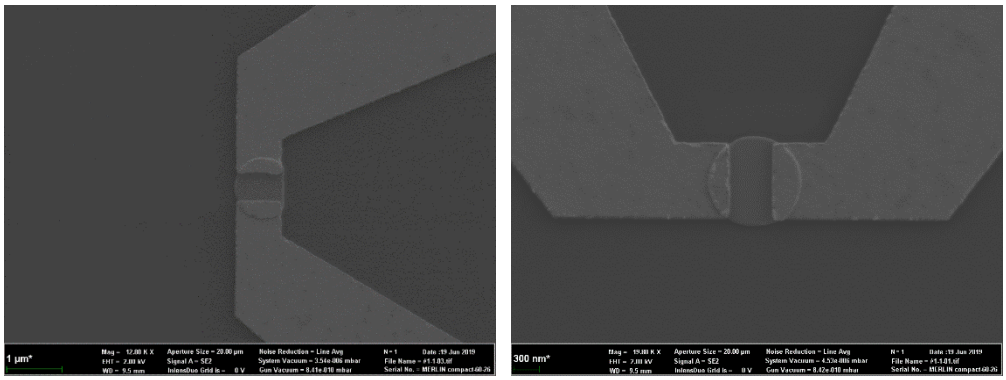

Fig. 5.2 Patterned Py disks and Au electrodes observed by SEM.

5.2. DC AMR measurement

A lock-in measurement technique is used to characterize the DC AMR behavior of the sample by flowing a constant current of 0.5mA through the magnetic sample. DC AMR curves for a circular disk and chopped disk sample made of Permalloy with lateral dimensions of 1000nm and 40nm thickness are shown in Fig. 5.4 (a), (b) as a function of strengths of the external DC magnetic fields. An external in-plane DC magnetic field is varied between -60mT and 60mT and the voltage drop across the magnetic sample is measured in a lock-in amplifier. Initially, we applied a DC magnetic field of 60mT along the Y (X) direction that is sufficient to saturate the magnetic element to bring it in a single domain state by aligning the individual magnetic moments parallel to (perpendicular to) the current flow direction. At higher magnetic fields, we can see that due to the AMR effect, the resistance of the sample is higher when magnetic field is applied parallel to the current flow direction (0 degree, $H_{ext} \parallel I$, red line) compared to the perpendicular case (90 degree, $H_{ext} \perp I$, blue line). The Zeeman energy changes while varying the strength of the external magnetic field. When the Zeeman energy becomes sufficiently small, the magnetization curls along the edges of the microstructures to minimize stray fields, leading to a flux closure arrangement. As the field strength is reduced the resistance of the sample changes which indicates a change in magnetization state of the sample. The vortex core reaches the center of the element at zero field resulting in a maximum or a minimum in the AMR curves. Now increasing the field strength in the other direction moves the vortex core away from the center of the disk. After a certain value of the external field, indicated by small but sharp jumps at positive fields the vortex core

escapes from the samples at the so-called annihilation field where the magnetic element transforms back into a single domain or into an onion state. After this point, there is no significant change in the voltage signal which indicates the saturation state in the other direction. The AMR curves show almost reversible non-symmetric curves and different magnetization processes can be investigated with these curves such as: the nucleation, the propagation and the annihilation of the vortex core. Therefore, this curves similarly follows the hysteresis loops of vortex-state disk shown in Fig. 5.5.

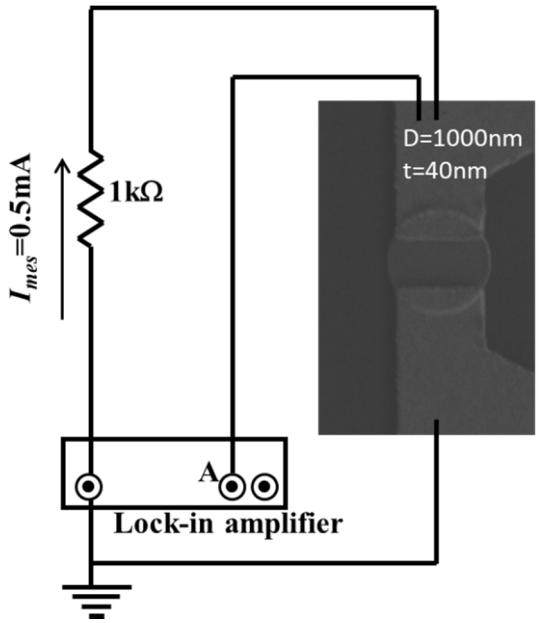

Fig. 5.3 The electrical measurement setup for DC AMR measurement

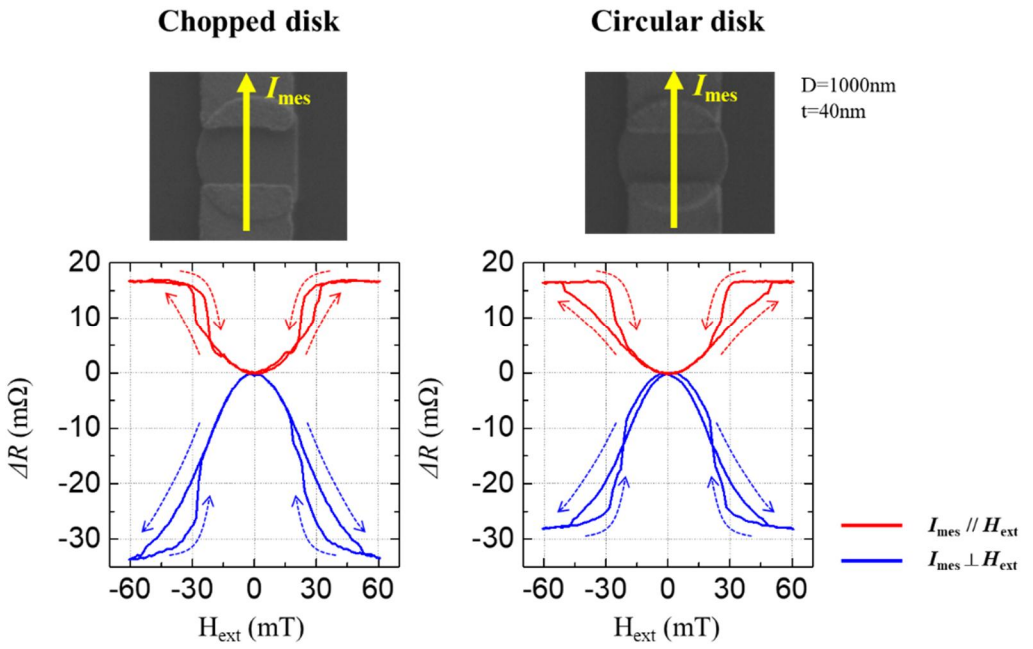

Fig. 5.4 Experimentally measured dc AMR curves for (a) a chopped disk and (b) a circular disk.

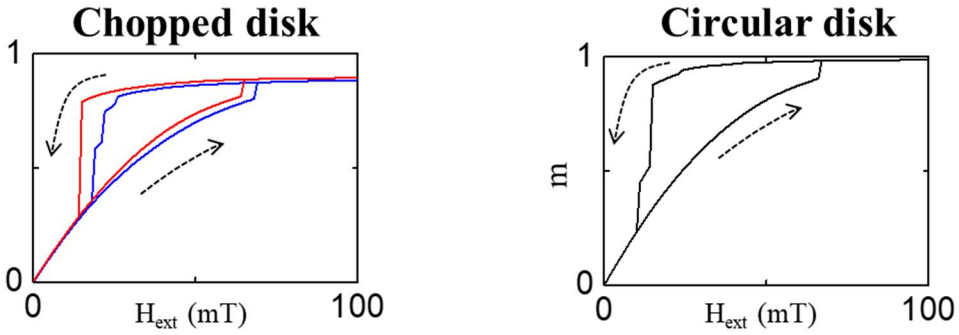

Fig. 5.5 The hysteresis loops of the (a) chopped disk and (b) circular disk by micromagnetic simulation.

5.3. AC AMR measurement by rectification technique

In this section, we present a conceptually simple technique to determine the dynamics of the vortex state electrically by exploiting the AMR effect where measurements. When an RF current $I = I_0 \cos(\omega \mathrm{t})$ flows through the vortex structure, as a result of the spin-transfer-torque exerted on the local magnetic moments, the vortex core starts to gyrate around its equilibrium position. Consequently, the magnetization configuration of the sample changes periodically with the position of the vortex core. Since the resistance of the ferromagnetic sample depends upon the relative orientation between the sample magnetization and the current flow direction, the gyrotropic motion of the vortex core is followed by a periodic change in the resistance of the magnetic sample. As the vortex core moves symmetrically around the center of the magnetic element, its resistance $R = R_0 + \Delta R \cos(2\omega t + \phi)$ changes with twice the frequency of the excitation current [106-109]. If the vortex core moves along the current flow direction, the effective magnetization of the sample is perpendicular to the direction of the current flow. Therefore, these two states have low resistance. In the other case, when the vortex core moves perpendicular to the current flow direction, the effective magnetization is along the current flow, so these two states have high resistance. Thus the resistance of the sample goes through high and low resistance states twice over a period of gyration, which means the periodicity of the resistance is twice to that of the RF current. This periodic resistance change combined with the RF current generates a homodyne voltage signal (indicating that the reference mixed signal is derived from the same source as the original signal, which has the advantage of being insensitive to the fluctuations in the frequency of the

original signal). This can be simply understood by following Ohm's law:

$$\begin{aligned} V &= I \times R \\ &= I\cos(\omega t) \times (R_0 + \Delta R\cos(2\omega t + \phi)) \\ &= IR_0\cos(\omega t) + \frac{1}{2} I\Delta R\{\cos(\omega t + \phi) + \cos(3\omega t + \phi)\} \end{aligned} \quad (3.3.1)$$

This homodyne signal can be measured by an oscilloscope and can be used to investigate the vortex dynamics. However, since electronic circuits can be deal easier with the DC signals compared to the RF signals, we are interested in the rectifying this homodyne voltage signal to measure the DC response. To obtain the rectified voltage signal, it is necessary to break the symmetry of the magnetic configuration to be able to generate a component in the oscillating resistance which is changing with the same frequency of the RF current. This can be achieved either by creating a defect in the magnetic disk or by moving the vortex core away from the center of the magnetic disk by applying an external DC magnetic field. In this case the resistance can be expressed as:

$$R = R_0 + \Delta R\sum_{n\neq 0} A_n \cos(n\omega t + \phi) \quad (3.3.2)$$

Here A_n are constant coefficients. This means that the oscillating resistance has a component at the excitation frequency $\Delta RA_1\cos(\omega t + \phi)$ which mixes with the RF current and generate a dc voltage signal as following:

$$\begin{aligned} V &= I \times R \\ &= V_0[\mathrm{B}_1\cos(\phi) + \sum_{n\neq 0} B_n \cos(n\omega t + \phi)] \\ &= V_{dc} + V_{ac} \end{aligned} \quad (3.3.3)$$

Here B_n are the constant coefficients. The rectified voltage signal, $V_{dc,}$ can simply be measured by a nanovoltmeter. Here we notice that the rectified signal is accompanied by the phase factor cos(φ). As described earlier, there is a phase difference of 180 degrees for the two polarities of the vortex core, thus we can expect that the sign of the rectified signal will be reversed when the vortex core polarity is switched without changing other parameters [106].

Fig. 5.7. shows the measured rectified voltages generated from the gyrotropic motion of the vortex core. We observed a peak appears near 378MHz which corresponds to the resonant frequency when the H_{ext} = 16.2mT for both samples. On the contrary, for the H_{ext} = -16.2mT case, a peak appears near 275MHz for a chopped disk and 378MHz for a circular disk. This result is well-matched with the resonance spectra obtained by simulation in the chapter 4.1.

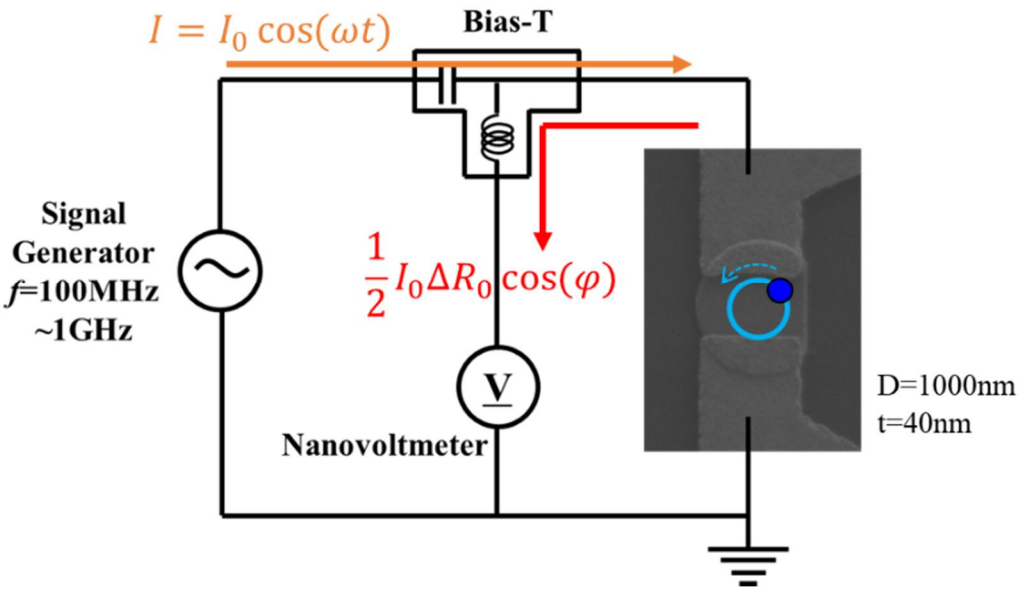

Fig. 5.6 The electrical measurement set-up for rectification measurement.

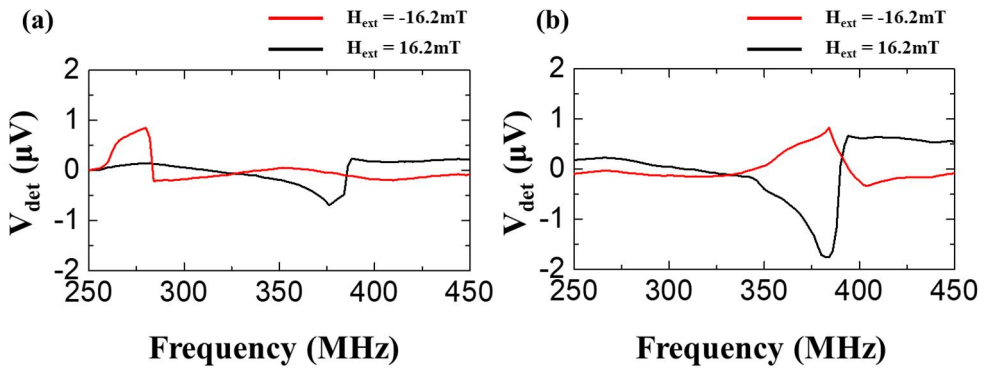

Fig. 5.7 The result of rectification measurement for (a) a chopped disk and (b) a circular disk.

To verify this electrically measured results, we calculated the rectified voltage from simulation results in the similar condition. For symmetric electrode placement on a disk the change in resistance is given by

$$R = R_0 + a_x X^2 - a_y Y^2 \quad (3.3.4)$$

where X and Y are the time-dependent core position with respect to the disk's center. We can extract the coefficients a_x and a_y from DC AMR measurement results, shown in Fig. 5.4. For the chopped disk, the ratio between these coefficients was about $a_x : a_y = 1 : 2.04$, and for the circular disk, it was about $a_x : a_y = 1 : 2.6$. The rectified voltage can be calculated by Ohm's law [106-109],

$$I(t) = I_0 \cos(\omega t)$$

$$V_{\det} = \lim_{T\to\infty} \frac{1}{T} \int_0^T I(t)R(t)dt \quad (3.3.5)$$

We calculated the rectified voltage from simulation result by using equation (3.2.4) and (3.2.5), as shown in Fig. 5.8. The resonant peaks have same signs at the same external fields, and have same lower shifting at H_{ext} = -16.2mT at the chopped disk case, but the resonant peaks differ in frequency compared to the experimental results. These resonant frequency differences can arise from the misalignment of the external field and the current direction, sample dimension differences, quality of Py thin films, and so on.

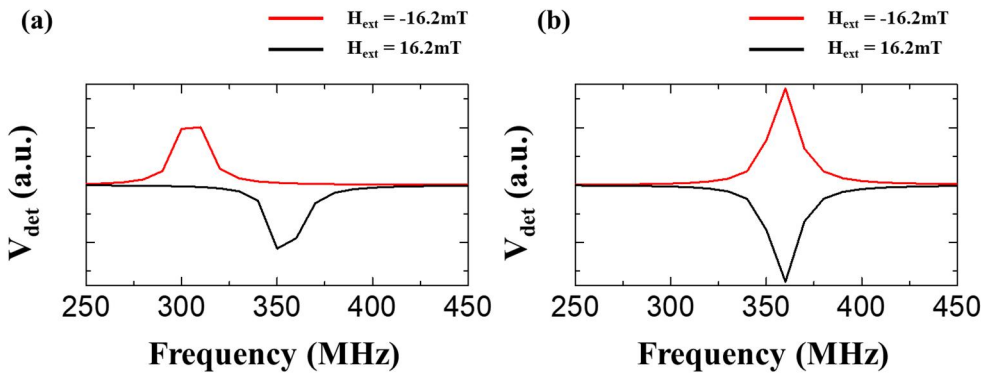

Fig. 5.8 The rectified voltage calculated from simulation data for (a) a chopped disk and (b) a circular disk.

Further, we measured rectified resonance spectra of the rectified voltage signal generated from the gyrotropic motion of the vortex core as a function of external fields, as shown in Fig. 5.9. As aforementioned, the resonant spectra of chopped disk and circular disk show different behavior as the external field decrease. These external field dependent spectra are also calculated by simulation results, as shown in Fig. 5.10, which is similar with the electrically measured results. Therefore, we could electrically measure the gyrotropic resonant mode of vortex core in both chopped disk and circular disk, and the results are verified by simulation.

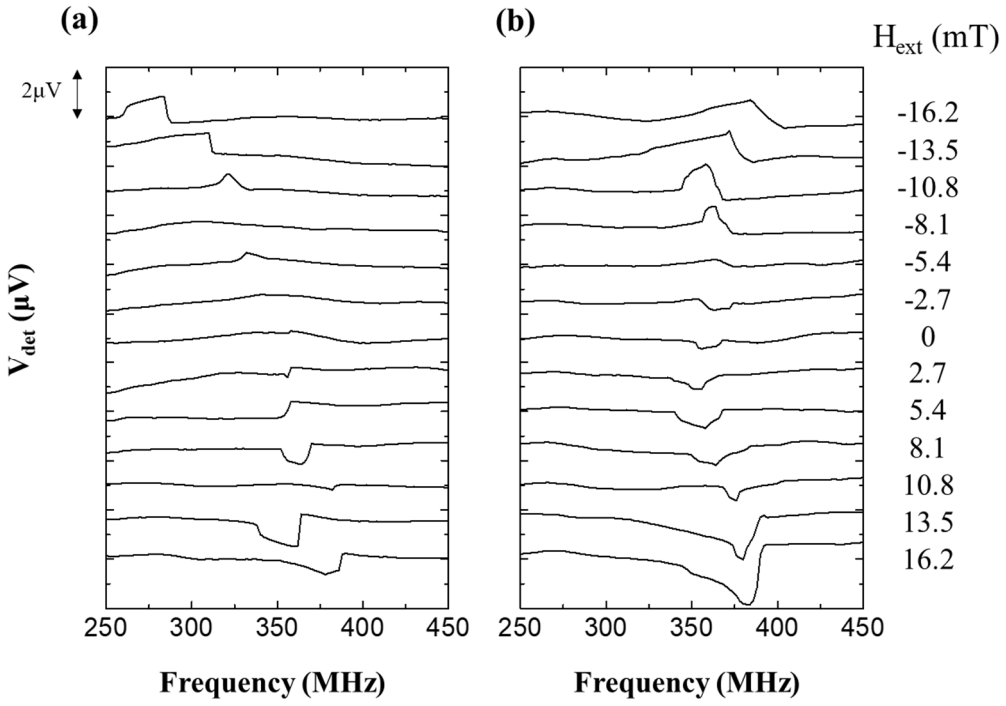

Fig. 5.9 The result of rectification measurement for (a) a chopped disk and (b) a circular disk as a function of bias fields.

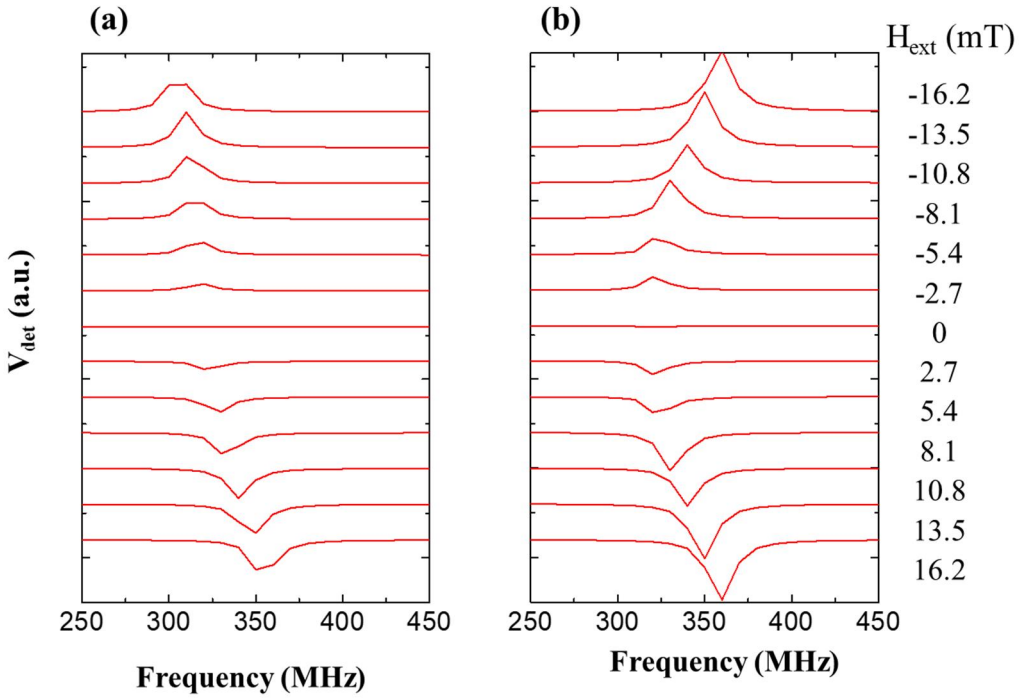

Fig. 5.10 The rectified voltage calculated from simulation data for (a) a chopped disk and (b) a circular disk as a function of bias fields.

6. Summary

In this thesis, the collective vortex-gyration in dipolar coupled arrays of magnetic disk is investigated by micromagnetic simulation. Furthermore, the electrical measurements of resonance gyrotropic modes of vortex core in two different shape of disks are presented.

In the first part, on the basis of combinations of novel dynamic characteristics in single vortex-state disks and their dipolar-coupled disks, an efficient alternative to the switching of vortex-core polarities is proposed, which is totally different from earlier-reported magnetic-field- or current-driven vortex-core switching. With this switching mechanism, a new-concept RS latch logic operation using vortex-state-disk networks is explored. A three-magnetic-disk array of coupled vortices is used to demonstrate RS latch logic. While currently existing RS latch logics, consisting of several transistors, are typically volatile, the vortex-network-based RS latch is non-volatile, of unlimited endurance, and low-power-consumptive when using a low-damping material and resonant excitations of specific coupled modes.

In the second part, the gyration signal propagation is studied in ferromagnetic disk array. The resonant frequency can either be strongly increased by shifting the core towards the disk's round edge or decreased by shifting the core towards the disk's flat edge in the chopped disk. With this resonant frequency tuning mechanism, we demonstrated the control method of gyration signal propagation in ferromagnetic disk array which contains two circular disks and one chopped disk. On the basis of this method, we conceptually devised time- and frequency-division demultiplexer devices based on the five-vortex-state disk array. These proposed low-damping vortices based

demultiplexer devices have enormous tunability by the external magnetic field or the shape of the magnetic elements.

In the last part, we studied the vortex core's gyrotropic motion in two different shape of disks by electrical measurement. The DC AMR characteristics of the vortex-state chopped disk and circular disk are measured. After that, the gyrotropic resonant mode of vortex-state disks are detected by means of rectification measurement. The results are verified by simulation results under the similar conditions.

Magnetic vortex has many advantages such as non-volitility, almost unlimited endurance, and low power operation. Furthermore, a rich tunablity of coupled vortices makes them adoptable as an alternative building blocks of future spintronics devices. This work can pave the way for possible implementation of logic and information processing devices based on magnetic-vortex-state networks.

Bibliography

[1] G. Binasch, P. Gr¨unberg, F. Saurenbach, and W. Zinn, Phys. Rev. B **39**, 4828 (1989).

[2] M. N. Baibich, J. M. Broto, A. Fert, F. N. Van Dau, F. Petroff, P. Etienne, G. Creuzet, A. Friederich, and J. Chazelas, Phys. Rev. Lett. **61**, 2472 (1988).

[3] S. S. P. Parkin, Appl. Phys. Lett. **61**, 1358 (1992).

[4] D. E. Heim, R. E. Fontana, C. Tsang, V. S. Speriosu, B. A. Gurney, and M. L. Williams, IEEE Trans. Magn. **30**, 316 (1994).

[5] B. N. Engel, J. Åkerman, B. Butcher, R. W. Dave, M. DeHerrera, M. Durlam, G. Grynkewich, J. Janesky, S. V. Pietambaram, N. D. Rizzo, J. M. Slaughter, K. Smith, J. J. Sun, and S. Tehrani, IEEE Trans. Magn. **41**, 132 (2005).

[6] S. S. P. Parkin, M. Hayashi, and L. Thomas, Science **320**, 190 (2008).

[7] V. V. Kruglyak, S. O. Demokritov, and D. Grundler. Magnonics, J. Phys. D: Appl. Phys. **43**, 264001 (2010).

[8] S. Barman, A. Barman and Y. Otani, J. of Phys. D: Appl. Phys. **43**, 335001 (2010).

[9] D. A. Allwood, G. Xiong, M. D. Cooke, C. C. Faulkner, D. Atkinson, N. Vernier, and R. P. Cowburn, Science **296**, 2003 (2002).

[10] A. Imre, G. Csaba, L. Ji, A. Orlov, G. H. Bernstein, and W. Porod, Science **311**, 205 (2006).

[11] V. S. Pribiag, I. N. Krivorotov, G. D. Fuchs, P. M. Braganca, O. Ozatay, J. C. Sankey,

D. C. Ralph, and R. A. Buhrman, Nat. Phys. **3**, 498 (2007).

[12] Q. Mistral, M. van Kampen, G. Hrkac, Joo-Von Kim, T. Devolder, P. Crozat, C. Chappert, L. Lagae, and T. Schrefl, Phys. Rev. Lett. **100**, 257201 (2008).

[13] A. Hubert and R. Schäfer, "Magnetic Domains - The Analysis of Magnetic Microstructures" (Springer, Berlin, New York, Heidelberg, 1998).

[14] T. Shinjo, T. Okuno, R. Hassdorf, K. Shigeto, and T. Ono, Science **289**, 930 (2000).

[15] A. Wachowiak, J. Wiebe, M. Bode, O. Pietzsch, M. Morgenstern, and R. Wiesendanger, Science **298**, 577 (2002).

[16] S.-B. Choe, Y. Acremann, A. Scholl, A. Bauer, A. Doran, J. Stöhr, and H. A. Padmore, Science **304**, 420 (2004).

[17] V. Novosad, F. Y. Fradin, P.E. Roy, K. S. Buchanan, K. Yu. Guslienko, and S. D. Bader, Phys. Rev. B **72**, 024455 (2005).

[18] S. Bohlens, B. Krüger, A. Drews, M. Bolte, G. Meier, and D. Pfannkuche, Appl. Phys. Lett. **93**, 142508 (2008).

[19] K. Nakano, D. Chiba, N. Ohshima, S. Kasai, T. Sato, Y. Nakatani, K. Sekiguchi, K. Kobayashi, and T. Ono, Appl. Phys. Lett. **99**, 262505 (2011).

[20] K. Tanabe, D. Chiba, J. Ohe, S. Kasai, H. Kohno, S. E. Barnes, S. Maekawa, K. Kobayashi, and T. Ono, Nat. Comm. **3**, 845 (2012).

[21] B. Pigeau, G. de Loubens, O. Klein, A. Riegler, F. Lochner, G. Schmidt, L. W. Molenkamp, V. S. Tiberkevich, and A. N. Slavin, Appl. Phys. Lett. **96**, 132506 (2010).

[22] J. Shibata, K. Shigeto, and Y. Otani, Phys. Rev. B **67**, 224404 (2003).

[23] J. Shibata, and Y. Otani, Phys. Rev. B **70**, 012404 (2004).

[24] Y. A. Galkin, B. A. Ivanov, and C. E. Zaspel, Phys. Rev. B **74**, 144419 (2006).

[25] S. A. Nikitov, Ph. Tailhades, and C.S. Tsai, J. Magn. Magn. Mater. **236**, 320 (2001).

[26] G. Gubbiotti, S. Tacchi, G. Carlotti, N. Singh, S. Goolaup, A. O. Adeyeye, and M. Kostylev, Appl. Phys. Lett. **90**, 092503 (2007).

[27] J. Topp, D. Heitmann, M. P. Kostylev, and D. Grundler, Phys. Rev. Lett. **104**, 207205 (2010).

[28] K.-S. Lee, D.-S. Han, and S.-K. Kim, Phys. Rev. Lett. 102, 127202 (2009).

[29] L.D.L. Landau, E.M., Phys. Z. Sowjetunion, Phys. Rev. **9**, 1935 (1935).

[30] W. F. Brown, Jr., "Micromagnetics" (Wiley, New York, 1963).

[31] T. L. Gilbert, IEEE Trans. Magn. **40**, 3443 (2004).

[32] S. K. Kim, J. Phys. D-Appl. Phys. **43**, 264004 (2010).

[33] A. Aharoni "Introduction to the Theory of Ferromagnetism" (Clarendon Press; Second Edition, 2000).

[34] J. D. Jackson, "Classical Electrodynamics (Second Ed.)" (John Wiley and Sons., 1975).

[35] J. Raabe, R. Pulwey, R. Sattler, T. Schweinböck, J. Zweck, and D. Weiss, J. Appl. Phys. **88**, 4437 (2000).

[36] T. Shinjo, T. Okuno, R. Hassdorf, K. Shigeto, and T. Ono, Science **28**, 930, (2000).

[37] M. E. Gouva, G. M. Wysin, A. R. Bishop, and F. G. Mertens, Phys. Rev. B **39**,11840, (1989).

[38] Jonathan Kin Ha, Riccardo Hertel, and J. Kirschner, Phys. Rev. B **67**, 224432 (2003).

[39] A. Wachowiak, J. Wiebe, M. Bode, O. Pietzsch, M. Morgenstern, and R. Wiesendanger, Science (New York, N.Y.) **298**, 577 (2002).

[40] J. Miltat and A. Thiaville, Science **298**, 555 (2002).

[41] R. P. Cowburn, J. Magn. Magn. Mater. **242**, 505 (2002).

[42] Stellan Bohlens, Benjamin Krüger, André Drews, Markus Bolte, Guido Meier, and Daniela Pfannkuche, Appl. Phys. Lett. **93**, 142508 (2008).

[43] Kunihiro Nakano, Kenji Tanabe, Ryo Hiramatsu, Daichi Chiba, Norikazu Ohshima, Shinya Kasai, Tomonori Sato, Yoshinobu Nakatani, Koji Sekiguchi, Kensuke Kobayashi, and Teruo Ono, Appl. Phys. Lett. **102**, 072405 (2013).

[44] Hauke H. Langner, Lars Bocklage, Toru Matsuyama, and Guido Meier, Phys. Rev. B **87**, 064420 (2013).

[45] E.R.P. Novais, A.P. Guimarães, arXiv:0909.5686 (2009).

[46] A. A. Thiele, Phys. Rev. Lett. **30**, 230 (1973).

[47] D. L. Huber, Phys. Rev. B **26**, 3758 (1982).

[48] J. Shibata, Y. Nakatani, G. Tatara, H. Kohno, and Y. Otani, Phys. Rev. B **73**, 020403

(2006).

[49] J. He, Z. Li, and S. Zhang, Phys. Rev. B **73**, 184408 (2006).

[50] N. Kikuchi, S. Okamoto, O. Kitakami, Y. Shimada, S. G. Kim, Y. Otani, and K. Fukamichi, J. Appl. Phys., **90**, 6548 (2001).

[51] André Thiaville, José Miguel García, Rok Dittrich, Jacques Miltat, and Thomas Schrefl, Phys. Rev. B **67**, 094410 (2003).

[52] V.P. Kravchuk and D.D. Sheka, Phys. Solid State **49**, 1923 (2007).

[53] R. Hertel, S. Gliga, M. Fähnle, and C. M. Schneide, Phys. Rev. Lett. **98**, 117201 (2007).

[54] Keisuke Yamada, Shinya Kasai, Yoshinobu Nakatani, Kensuke Kobayashi, Hiroshi Kohno, Andre Thiaville, and Teruo Ono, Nat. Mater. **6**, 270 (2007).

[55] Y. B. Gaididei, V. P. Kravchuk, D. D. Sheka, and F. G. Mertens, Low Temp. Phys. **34**, 528 (2008).

[56] Yuri Gaididei, Till Kamppeter, Franz G. Mertens, and A. R. Bishop, Phys. Rev. B **61**, 9449 (2000).

[57] A. S. Kovalev and J. E. Prilepsky, Low Temp. Phys. **28**, 921 (2002).

[58] J. P. Zagorodny, Y. Gaididei, F. G. Mertens, and A. R. Bishop, Eur. Phys. J. B **31**, 471 (2003).

[59] V. Novosad, K. Yu. Guslienko, H. Shima, Y. Otani, S. G. Kim, K. Fukamichi, N.

Kikuchi, O. Kitakami, and Y. Shimada, Phys. Rev. B **65**, 060402 (2002).

[60] M. Bolte, R. Eiselt, G. Meier, D.-J. Kim, and P. Fischer, J. Appl. Phys. **99**, 08H301 (2006).

[61] G. Gubbiotti, M. Madami, S. Tacchi, G. Carlotti, and T. Okuno, J. Appl. Phys. **99**, 08C701 (2006).

[62] J. Shibata, K. Shigeto, and Y. Otani, J. Magn. Magn. Mater. **272**, 1688 (2004).

[63] K. S. Lee, H. Jung, D. S. Han, and S. K. Kim, J. Appl. Phys. **110**, 113903 (2011).

[64] A. Barman, S. Barman, T. Kimura, Y. Fukuma, and Y. Otani, J. Phys. D-Appl. Phys. **43**, 422001 (2010).

[65] S. Barman, A. Barman, and Y. Otani, IEEE Trans. Magn. **46**, 1342 (2010).

[66] H. Jung, Y.-S. Yu, K.-S. Lee, M.-Y. Im, P. Fischer, L. Bocklage, A. Vogel, M. Bolte, G. Meier, and S.-K. Kim, Appl. Phys. Lett. **97**, 222502 (2010).

[67] A. Vogel, A. Drews, T. Kamionka, M. Bolte, and G. Meier, Phys. Rev. Lett. **105**, 037201 (2010).

[68] H. Jung, K.-S. Lee, D.-E. Jeong, Y.-S. Choi, Y.-S. Yu, D.-S. Han, A. Vogel, L. Bocklage, G. Meier, M.-Y. Im, P. Fischer and S.-K. Kim, Sci. Rep. **1**, 59 (2011).

[69] A. Vogel, M. Martens, M. Weigand, and G. Meier, Appl. Phys. Lett. **99**, 042506 (2011)

[70] A. Vogel, T. Kamionka, M. Martens, A. Drews, K. W. Oll, T. Tyliszczak, H. Stoll, B.

Van Waeyenberge, and G. Meier, Phys. Rev. Lett. **106**, 137201 (2011).

[71] S. Sugimoto, Y. Fukuma, S. Kasai, T. Kimura, A. Barman, and Y. Otani, Phys. Rev. Lett. **106**, 197203 (2011).

[72] J.-H. Kim, K.-S. Lee, H. Jung, D.-S. Han, and S.-K. Kim, Appl. Phys. Lett. **101**, 092403 (2012).

[73] H. Jung, Y.-S. Choi, K.-S. Lee, D.-S. Han, Y.-S. Yu, M.-Y. Im, P. Fischer, and S.-K. Kim, ACS Nano **6**, 3712 (2012).

[74] S. Jain, V. Novosad, F. Y. Fradin, J. E. Pearson, V. Tiberkevich, A. N. Slavin, and S., D. Bader, Nat. Comm. **3**, 1330 (2012).

[75] A. Vogel, A. Drews, M. Weigand, and G. Meier, AIP Advan. **2**, 042180 (2012).

[76] N. Locatelli, V. V. Naletov, J. Grollier, G. de Loubens, V. Cros, C. Deranlot, C. Ulysse, G. Faini, O. Klein and A. Fert, Appl. Phys. Lett. **98**, 063501 (2011).

[77] A. Y. Galkin, B. A. Ivanov, and C. E. Zaspel, Phys. Rev. B **74**, 144419 (2006).

[78] O. V. Sukhostavets, J. Gonzalez, and K. Y. Guslienko, Phys. Rev. B **87**, 094402 (2013).

[79] C. Mack, "Fundamental Principles of Optical Lithography: The Science of Microfabrication" (John Wiley & Sons 2007).

[80] W. Thomson, Proceedings of the Royal Society of London **8**, 546 (1856).

[81] R. M. Bozorth, Phys. Rev. **70**, 923 (1946).

[82] J. Smit, Physica **17**, 612 (1951).

[83] L. Berger, Physica **30**, 1141 (1964).

[84] T. R. McGuire and R. I. Potter, IEEE Transactions on, **11**, 1018 (1975).

[85] N. F. Mott, Proceedings of the Royal Society A **153**, 699 (1936).

[86] J. Holanda, D. S. Maior, A. Azevedo, S. M. Rezende, J. Magn. Magn. Mater. **432**, 507 (2017).

[87] B. Van Waeyenberge, A. Puzic, H. Stoll, K. W. Chou, T. Tyliszczak, R. Hertel, M. Fähnle, H. Brückl, K. Rott, G. Reiss, I. Neudecker, D. Weiss, C. H. Back, and G. Schütz, Nature **444**, 461 (2006).

[88] K. Yamada, S. Kasai, Y. Nakatani, K. Kobayashi, H. Kohno, A. Thiaville, and T. Ono, Nat. Mater. **6**, 270 (2007).

[89] Y.-S. Yu, H. Jung, K.-S. Lee, P. Fischer, and S.-K. Kim, Appl. Phys. Lett. **98**, 052507 (2011).

[90] S. Bohlens, B. Krüger, A. Drews, M. Bolte, G. Meier, and D. Pfannkuche, Appl. Phys. Lett. **93**, 142508 (2008).

[91] B. Pigeau, G. de Loubens, O. Klein, A. Riegler, F. Lochner, G. Schmidt, L. W. Molenka mp, V. S. Tiberkevich, and A. N. Slavin, Appl. Phys. Lett. **96**, 132506 (2010).

[92] Q. F. Xiao, J. Rudge, B. C. Choi, Y. K. Hong, and G. Donohoe, Appl. Phys. Lett. **89**, 262507 (2006).

[93] Y. Liu, S. Gliga, R. Hertel, and C. M. Schneider, Appl. Phys. Lett. **91**, 112501 (2007).

[94] R. Hertel, S. Gliga, M. Fähnle, and C. M. Schneider, Phys. Rev. Lett. **98**, 117201 (2007).

[95] S.-K. Kim, K.-S. Lee, Y.-S. Yu, and Y.-S. Choi, Appl. Phys. Lett. **92**, 022509 (2008).

[96] M. Curcic, B. Van Waeyenberge, A. Vansteenkiste, M. Weigand, V. Sackmann, H. Stoll, M. Fähnle, T. Tyliszczak, G. Woltersdorf, C. H. Back, and G. Schütz, Phys. Rev. Lett. **101**, 197204 (2008).

[97] Y.-S. Choi, M.-W. Yoo, K.-S. Lee, Y.-S. Yu, H. Jung, and S.-K. Kim, Appl. Phys. Lett. **96**, 072507 (2010).

[98] J.-G. Caputo, Y. Gaididei, F. G. Mertens, and D. D. Sheka, Phys. Rev. Lett. **98**, 056604 (2007).

[99] J. Kim and S.-K. Kim, J. Magn. **22**, 29 (2017).

[100] N. Papanicolaou and T. N. Tomaras, Nucl. Phys. B **360**, 425 (1991).

[101] D.-S. Han, A. Vogel, H. Jung, K.-S. Lee, M. Weigand, H. Stoll, G. Schütz, P. Fischer, G. Meier, and S.-K. Kim, Sci. Rep. **3**, 2262 (2013).

[102] K.-S. Lee, S.-K. Kim, Y.-S. Yu, Y.-S. Choi, K. Y. Guslienko, H. Jung, and P. Fischer, Phys. Rev. Lett. **101**, 267206 (2008).

[103] K. S. Buchanan, P. E. Roy, M. Grimsditch, F. Y. Fradin, K. Y. Guslienko, S. D. Bader, and V. Novosad, Phys. Rev. B **74**, 064404 (2006).

[104] M. Sushruth, J. P. Fried, A. Anane, S. Xavier, C. Deranlot, V. Cros, and P. J. Metaxas, Phys. Rev. B **96**, 060405(R) (2017).

[105] D. Kumar, S. Barman and A. Barman, Sci. Rep. **4**, 4108 (2014).

[106] A. Gangwar, H. G. Bauer, J.-Y. Chauleau, M. Noske, M. Weigand, H. Stoll, G. Schütz, and C. H. Back, Phys. Rev. B **91**, 094407 (2015).

[107] M. Goto, H. Hata, A. Yamaguchi, Y. Nakatani, T. Yamaoka, Y. Nozaki, and H. Miyajima, Phys. Rev. B **84**, 064406 (2011).

[108] X. Cui, S. Hu, M. Hidegara, S. Yakata and T. Kimura, Sci. Rep. **5**, 17922 (2015).

[109] M. Sushruth, J. P. Fried, A. Anane, S. Xavier, C. Deranlot, M. Kostylev, V. Cros, and P. J. Metaxas, Phys. Rev. B **94**, 100402(R) (2016).

Publication List

1. D.-S. Han, Y.-J. Cho, H.-B. Jung and S.-K. Kim, J. Appl. Phys. 117, 083910 (2015).

   “Perpendicular-bias-field control of coupled-vortex oscillations in nanodot networks”

2. J. Yang, J. Kim, B. Kim, Y.-J. Cho, J.-H. Lee, and S.-K. Kim, Physical Review B 94, 024425 (2016).

   “Characteristic dynamic modes and domain-wall motion in magnetic nanotubes excited by resonant rotating magnetic fields”

3. J. Kim, J. Yang, Y.-J. Cho, B. Kim, and S.-K. Kim, Sci. Rep. 7, 45185 (2017).

   “Coupled gyration modes in onedimensional skyrmion arrays in thin-film nanostrips as new type of information carrier”

4. B. Bhoi, B. Kim, J. Kim, Y.-J. Cho and S.-K. Kim, Sci. Rep. 7,11930 (2017).

   “Robust magnon-photon coupling in a planar-geometry hybrid of inverted split-ring resonator and YIG film”

5. J. Yang, J. Kim, B. Kim, Y.-J. Cho, J.-H. Lee, and S.-K. Kim, J. Appl. Phys. 123, 033901 (2018).

   “Vortex-chirality-dependent standing spin-wave modes in soft magnetic nanotubes”

6. J. Kim, J. Yang, Y.-J. Cho, B. Kim, and S.-K. Kim, J.Appl. Phys. 123, 053903 (2018).

"Coupled breathing modes in one-dimensional Skyrmion lattices"

7. B. Kim, Y.-J. Cho, B. Bhoi, S.-Y. Park, and S.-K. Kim, J. Magn. Magn. Mater. 465, 399 (2018).
"Hetero-interface effect on Gilbert damping in nonmagnetic metal/permalloy/nonmagnetic metal trilayers"

8. Y.-J. Cho and S.-K. Kim, AIP Advances **9**, 055028 (2019).
"Reset-set latch logic operation using vortex-gyration-coupled modes and its driven switching in magnetic-dot networks: A micromagnetic simulation study"

Patent List

1. “자성 박막 구조체를 이용한 논리 소자 및 이의 동작 방법”

   S.-K. Kim, Y.-J. Cho, Korea Patent 10-2019-0045081

Presentations in Conferences

1. [2014] 한국자기학회 2014 동계학술대회

   Dong-Soo Han, Young-Jun Cho, Hanbyeol Jeong, Sang-Koog Kim

   “Perpendicular-bias-field control of coupled-vortex oscillations in nanodotnetworks”

2. [2018] The 5th International Conference of Asian Union of Magnetics Societies,

   Young-Jun Cho, Junhoe Kim, Jae-Hyeok Lee, Jaehak Yang, Bosung Kim, and Sang-Koog Kim

   “Vortex-polarity Switching in Magnetic-dot Arrays by Gyration Signals”

3. [2018] 한국자기학회 2018 동계학술대회

   Young-Jun Cho and Sang-Koog Kim

   “Vortex-polarity switching in magnetic-dot arrays by gyration signals and its application to SR latch”

4. [2019] 한국자기학회 2019 하계학술대회

   Young-Jun Cho, Jaegun Sim and Sang-Koog Kim

   “In-plane field control of coupled-vortex oscillations in magnetic-dot-networks”

국문 초록

자성 디스크 배열 내 결합된 자기 소용돌이의 동적 거동 연구

자기 소용돌이는 수 마이크로미터 크기 혹은 그 이하의 강자성 구조체에서 안정적으로 형성되는 특이한 배열 구조를 말한다. 자기 소용돌이는 박막면에 수직한 수십 나노미터 크기의 자기 소용돌이 핵과, 그 주위의 평면 내 회전하는 모양으로 배열된 스핀들로 구성된다. 자기 소용돌이에 외부 자기장 혹은 전류 등을 인가하면 자기 소용돌이 핵이 회전운동을 하는 성질이 있다. 이러한 자기 소용돌이는 핵의 두 가지 자화방향과 주변에 배열된 스핀들의 두 가지 회전방향의 조합으로 네 개의 동일한 기저 에너지 준위를 가질 수 있고, 열적으로 매우 안정하기 때문에 비휘발성 정보저장 소자로 응용 가능하다. 또한 여러 개의 결합된 자기 소용돌이 사이에서 나타나는 자기 소용돌이 핵의 집단적 회전운동은 새로운 신호전달의 매개체로 이용될 수 있어 정보처리 소자로의 응용성에 대한 연구가 진행되어왔다.

본 학위 논문에서는 미소자기 전산모사 및 실험을 이용하여 자기 소용돌이의 동적 거동과 자기 소용돌이 간의 동적 상호작용 연구에 초점을 두고있다. 자기 디스크 배열에서 자기 소용돌이 결합 모드, 자기 소용돌이 핵 반전 방법 및 자기 소용돌이 핵의 회전운동 신호 전달의 제어에 관한 연구가 주 내용이

다. 이러한 자기 소용돌이의 동적 거동 제어 방법을 이용해 새로운 개념의 RS 래치 논리 소자, 시분할 및 주파수 분할 디멀티플렉서 소자를 제안하고 그 동작 특성을 연구하였다. 자기 소용돌이를 이용한 소자들은 비휘발성이며, 거의 무제한의 수명을 가지고, 에너지가 적게 드는 등 많은 장점을 가지고 있다. 또한 자기 소용돌이는 그 특성의 제어가 매우 용이해서 향후 개발될 스핀트로닉스 소자로 응용될 수 있는 가능성을 가지고 있다. 본 연구 결과는 차세대 스핀트로닉스 기술로서 자기 소용돌이에 기반한 논리 소자 및 정보 처리 장치의 구현 가능성을 보여준다.

주요어: 자기 소용돌이, 자기 소용돌이 동역학, 결합된 역학, 자화 반전, 스핀 동역학, 마그논 결정, 스핀파, 스핀트로닉스

학번: 2012-30920